MCNP5 MONTE CARLO BASED DOSIMETRY FOR THE NUCLETRON IRIDIUM-192 HIGH DOSE-RATE BRACHYTHERAPY SOURCE WITH TISSUE HETEROGENEITY CORRECTIONS

by

Ramsés Herrera

A Thesis Submitted to the Faculty of

The Charles E. Schmidt College of Science

in Partial Fulfillment of the Requirements for the Degree of

Master of Science

Florida Atlantic University

Boca Raton, Florida

August 2012

MCNP5 MONTE CARLO BASED DOSIMETRY FOR THE NUCLETRON IRIDIUM-192 HIGH DOSE-RATE BRACHYTHERAPY SOURCE WITH TISSUE HETEROGENEITY CORRECTIONS

by

Ramsés Herrera

This thesis was prepared under direction of the candidate's thesis advisor, Silvia Pella, Ph.D., DABR, Research Affiliate Professor, Department of Physics, and has been approved by the members of his supervisory committee. It was submitted to the faculty of the Charles E. Schmidt College of Science and was accepted in partial fulfillment of the requirements for the degree of Master of Science.

SUPERVISORY COMMITTEE:

Silvia Pella, Ph.D., DABR
Thesis Advisor

Theodora Leventouri, Ph.D.

David G. Saez, M.S.

Andy W.C. Lau, Ph.D.

Warner A. Miller, Ph.D.
Chair, Department of Physics

Gary W. Perry, Ph.D.
Dean, Charles E. Schmidt College of Science

Barry T. Rosson, Ph.D.
Dean, Graduate College

July 16, 2012
Date

ACKNOWLEDGEMENTS

The author would like to express his most sincere gratitude to his Thesis Advisor, Medical Physicist Dr. Silvia Pella and Thesis Committee members Dr. Theodora Leventouri and Medical Physicist David G. Saez, for their guidance in the completion of this project. The author wishes to particularly thank Mr. Saez for his tireless efforts, without his input and guidance this project would have never come to fruition. I would also like to thank my colleagues in the Professional Masters in Medical Physics program, and Michael G. Stabin, Ph.D., Mark J. Rivard, Ph.D., Andy Schwarz, M.S., and David Medich, Ph.D. for their help during the development of the Monte Carlo input files.

ABSTRACT

Author:	Ramsés Herrera
Title:	MCNP5 Monte Carlo based Dosimetry for the Nucletron Iridium-192 High Dose-Rate Brachytherapy Source with Tissue Heterogeneity Corrections
Institution:	Florida Atlantic University
Thesis Advisor:	Silvia Pella, Ph.D., DABR
Degree:	Master of Science
Year:	2012

A Monte Carlo model has been developed using MCNP5 to simulate the Nucletron Ir-192 HDR source in order to investigate the influence of tissue heterogeneities on dose calculations compared to the dose in homogeneous water media, as it is typically calculated by brachytherapy Treatment Planning Systems (TPS). Validity of the simulation was verified in water medium in comparison with peer reviewed results using the dosimetric parameters recommended by AAPM, Task Group-43. The dose-rates in simulated prostate, bladder and rectum were compared to those obtained in the homogeneous water phantom. Based on the resulting dose differences, it is inferred that TPS algorithms for brachytherapy dose calculations overestimate the dose to tissues like prostate and bladder by up to 49%. A clinically relevant dose underestimation of 5.5% to the rectum was also found. We recommend that further

investigation using actual patient CT data as input to the Monte Carlo simulation be performed.

DEDICATION

I dedicate this Thesis to my family, specially my mother, Dixiana Pildain, my father Lorenzo Inocente Herrera León, Ph.D., and my stepfather Carlos Jesùs Pildain and my fiancée Jamie Leigh Baltra. You have been my support and my inspiration; all my achievements are because of your efforts and selfless sacrifice.

MCNP5 MONTE CARLO BASED DOSIMETRY FOR THE NUCLETRON IRIDIUM-192 HIGH DOSE-RATE BRACHYTHERAPY SOURCE WITH TISSUE HETEROGENEITY CORRECTIONS

LIST OF TABLES

LIST OF FIGURES

1.0 INTRODUCTION

1.1 OBJECTIVE

The main objective of the research presented in this Thesis is to develop a Monte Carlo simulation of dosimetric calculations for the Nucletron Ir^{192} High Dose-Rate brachytherapy source, utilizing the Monte Carlo N-Particle version 5 (MCNP5) software package. The Monte Carlo model seeks to investigate dosimetry in mediums other than water for one dwell position. This is in order to quantify and evaluate the influence of tissue heterogeneities created in a virtual phantom, for clinical brachytherapy calculations. This study may be beneficial for future investigations that aim to correct discrepancies in calculated doses by the Treatment Planning System (TPS) and actual doses received by the patient.

1.2 MOTIVATION(S)

1. The primary motivation for this Thesis is the creation of a Monte Carlos model that simulates an actively and widely used High Dose-Rate brachytherapy source.
2. Validation of the Monte Carlo model against the published values of TG-43 and other peer-reviewed models.

3. Deviate from the established model used in current Treatment Planning System (TPS), where a uniform medium of water is used, and introduce organ heterogeneities to investigate their influence on clinical doses. Of particular interest are the doses received by the rectum and bladder during treatment of the prostate.

1.3 RADIATON THERAPY

Radiation therapy is the term used to describe the delivery of ionizing radiation as part of a cancer treatment, with the aim of killing or controlling the growth of malignant cells. Radiation therapy can take any of two forms, *Curative* or *Palliative.* The intent of the therapy will be determined depending on the type of malignancy and/or the overall health of the patient.

1. *Curative Therapy:* This entails the use of radiation therapy as the primary method of treatment. It is usually used in certain cancers that are well localized to a specific area of the patient body, or after surgical removal of a cancer, to prevent tumor recurrence from microscopic metastases.
2. *Palliative Therapy:* This is the used of radiation therapy for symptomatic relief or local disease control whenever a total cure cannot be achieved.

1.3.1 RADIATION THERAPY MODALITIES

There are three main modalities of radiation therapy – *External Beam or Teletherapy, Radioisotope therapy* and *Brachytherapy* – each of which can be

used in either curative, palliative or adjuvant treatments with chemotherapy. Each therapy modality differs from the other by the type of radiation source used and the position of the radiation source with respect to the malignancy to be treated.

External Beam Therapy refers to the use of x-rays generated external to the patient in order to treat a malignancy. The usual method of treatment is through a Linear Accelerator (LINAC), capable of producing both, x-ray beams to treat deep seated tumors, and electron beams for lesions at or near the skin surface. A less commonly used treatment method involves the use of a collimated beam from the γ-ray decay of Co^{60}.

Figure 1: Simulated patient laying in a Varians TrueBeam external beam therapy Linear Accelerator. Image has been reproduced with permission from Varians Inc.

Radioisotope therapy is a form of targeted therapy where tumor targeting is accomplished by the chemical properties of the radioisotope or the pharmaceutical that is chemically attached to the radioisotope, *i.e.,* metaiodobenzylguanidine (MIBG), for the treatment of neuroblastoma. The

radio-pharmaceutical is delivered into the body through an infusion into the bloodstream or through oral ingestion and is distributed throughout the entire patient. Currently, radioisotope therapy is mostly used for the treatment of bone metastases with Strontium-89 (Sr^{89}), due to Strontium's Calcium chemical like behavior in the body, and Iodine-131 (I^{131}) in the treatment of metastatic neuroblastoma[1] and thyroid ablation.

The word brachytherapy has its origin in the Greek word *brachy (βραχύς)* - meaning "short-range." In this form of radiotherapy a sealed radionuclide source(s) is placed near *(intracavitary)* or implanted directly into the area requiring treatment *(interstitial)*.

The precise placement of the radioactive source near the site of the tumor means that toxicity is limited to a very well defined area – namely the tumor or lesion, with the surrounding normal tissue being well spared from radiation because of the *inverse square* drop-off in intensity as we move away from source. The highly localized delivery of radiation is the characteristic of brachytherapy that provides an added advantage over *External Beam Radiotherapy*. Because of the high degree of localization, brachytherapy is able to treat with very high doses of radiation, using the radiobiological advantage of late responding normal tissue, thus creating cure rates similar to surgery and *External Beam Radiation Therapy*[2,3,4,5].

Figure 2: Nucletron microSelectron digital HDR afterloader with back-up power supply, used for the computer controlled delivery of high dose-rate brachytherapy. Reproduced with permission from Eric J. Hall

The first use of a brachytherapy technique was in 1901, when physicist Pierre Curie suggested to physician Henri-Alexandre Danos the insertion of Radium tubes into a tumor – this was found to cause the tumor to shrink[6]. Brachytherapy techniques began to mature in the earlier part of the twentieth century, at the Curie Institute in Paris, France and St. Luke's and Memorial Hospital in New York, where the first techniques were developed[6,7]. The use of brachytherapy began to wane off in the mid twentieth century, after spill-over technology from World War II allowed for the development of external beam techniques that resulted in lower exposure to the non-patient personnel, while achieving good

tumor control. However, there is currently a resurgence in the use of brachytherapy due to its higher dosage to the tumor, more effective sparing of healthy tissues, and the recent development of afterloading techniques that allow the accurate, computer controlled delivery of radiation without exposure to anyone but the patient, by use of an afterloader device (Figure 2.).

Brachytherapy is categorized into three main treatment types, defined according to the rate of irradiation: *Low Dose Rate (LDR: up to 2 Gy/hr.) Medium Dose Rate (MDR: ≥2 Gy/hr & ≤ 12 Gy/hr) and High Dose Rate (HDR: over 12Gy/hr.).* Currently the main uses of brachytherapy are for the treatment of:

1. Prostate cancer via both, interstitial *HDR* and *LDR.*
2. Breast cancer with *HDR* techniques.
3. Skin cancer with *HDR* techniques.
4. Gynecological and cervical cancer with *HDR.*

1.4 DOSIMETRY FOR BRACHYTHERAPY SOURCES

1.4.1 SOURCE STRENGTH

All brachytherapy sources are encapsulated radionuclides whose activity, or rather kerma strength decays exponentially with time according to the decay equation: $S_K(t) = S_{K,o} e^{-\lambda_t (t)}$, where $S_K(t)$ is the Kerma strength at time t, $S_{K,o}$ is the initial source strength at time $t = 0$, and λ_t is the decay constant of the used isotope.

Before any dosimetric considerations can be made we must have a method of defining what entails the kerma strength S_K of a source and of determining what that strength is. The AAPM's Task Group 43 (TG-43)[8,9,10] concerns itself with the dosimetry of all brachytherapy sources as well as the definition of source strength. TG-43's definition of source strength is concurrent with that of ICRU 38 and ICRU 60[11] - $S_K = \dot{K}_\delta(d)d^2$ where $\dot{K}_\delta(d)$ is the kerma rate at a distance d that excludes all photons of energy below δ.

For the purpose of radiation therapy, the source strength is expressed in terms of Air-kerma strength with units $1U = 1\mu Gy\, m^2\, h^{-1}$. Air-kerma strength is the air-kerma rate, $\dot{K}_\delta(d)$, measured *in vacuo*, for energies higher than δ (the recommended value for brachytherapy sources is $\delta = 10KeV$) at a distance d, multiplied by the square of the distance[9]. The distance is taken from the center of the source and must be large relative to the maximum linear dimensions of the activity distribution, such that S_K is independent of d^2. This is usually obtained from measurements in the transverse plane of the source at a distance of one meter (Figure 3.) Although S_K is defined as measured *in vacuo*, the measurements are seldom made in this manner; rather, they are corrected for photon attenuation and scattering in air and any other medium that may be present between the source and the detector. Measurements of source strength for brachytherapy sources must be extremely accurate and are conducted by the

National Institute of Standards and Technology (NIST) or a laboratory whose calibration can be directly traced to NIST.

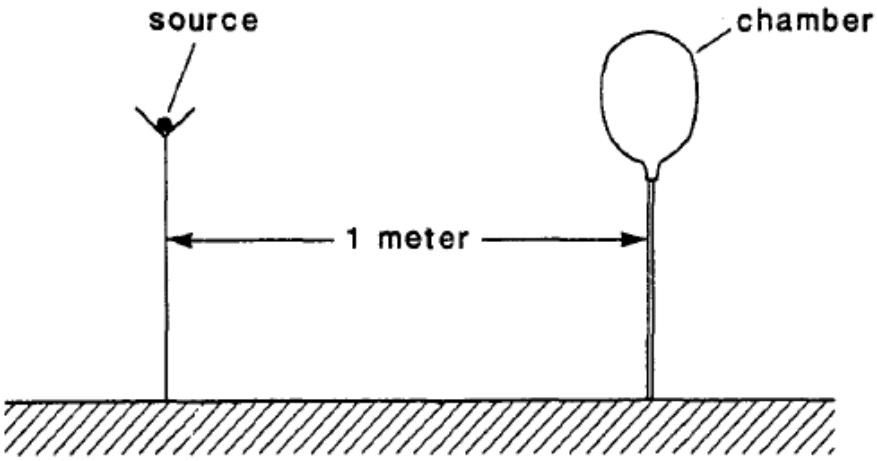

Figure 3: Schematic depiction for the Air-Kerma strength rate calibration of a brachytherapy source in open air. The image has been reproduced with permission from the publisher Lippincott Williams & Wilkins.

1.4.2 DOSIMETRIC PARAMETERS

Before a source can be clinically used its complete dosimetry must be known – that is, the absorbed dose in the patient, after a timed exposure, must be accurately assessed. The dosimetry for a brachytherapy source, defined by TG-43, is given by:

$$\dot{D}(r,\theta) = S_K \Lambda \frac{G_L(r,\theta)}{G_L(r_o,\theta_o)} g_L(r) F(r,\theta)$$

Where $\dot{D}(r,\theta)$ is the dose rate at a point of interest at distance *r* away from the source (Figure 4.) Each of the dosimetric parameters must be individually measured and are paramount to the overall accuracy of the clinical calculation, thus they are herein individually described.

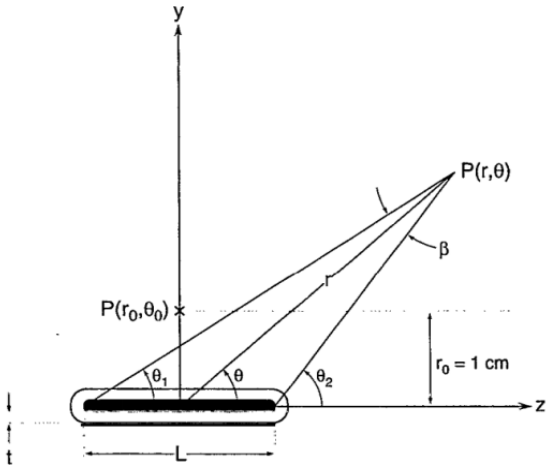

Figure 4: Coordinate system and geometric relationship used for calculation of brachytherapy dosimetry at a point P, from a line source. Image has been reproduced with the permission of the AAPM.

The Dose-Rate constant, Λ, is defined as the dose in a water medium at a distance of 1 cm in the transverse axis of a unit air-kerma strength source. The dose–rate constant, unlike the other dosimetric parameters for determining the

dose-rate of a brachytherapy source, is a relative measurement and will change in dependence to how the source strength, S_K, is calculated, as demonstrated in the equation below. This constant includes the effects of the internal distribution of radioactive material, the geometry of the encapsulation and the 'filtration' caused by the encapsulating material[8,9].

$$\Lambda = \frac{\dot{D}(r_o, \theta_o)}{S_K}$$

Brachytherapy sources are approximately cylindrical in shape; hence a direct *inverse-square law* for a dose fall-off approximation cannot be applied in the dosimetry. The Geometric Function provides an effective *inverse-square law* correction without taking into account the effects of scattering and attenuation. "Instead it is based upon an approximate model of the spatial distribution of radioactivity within the source[9]." Since the Geometric Function is used to obtain an interpolation between pre-calculated dose-rate values at specific distances, the cylinder approximation can be used without loss of accuracy. The geometric function, for a line-source approximation is:

$$G_L = \begin{cases} \dfrac{\beta}{L r \sin\theta} & \text{if } \theta \neq 0^\circ \\ \text{Or} \quad G_L = \left(r^2 - L^2/4\right)^{-1} & \text{if } \theta = 0^\circ \end{cases}$$

Where β is the angle (in radians) subtended by the ends of an imaginary line source with respect to the calculation point, $P(r, \theta)$ - (Figure. 4), and *L* is the radioactive length of the source.

Complementary to the geometric function, the Radial Dose function, $g_L(r)$ accounts for the dose fall-off in the transverse plane of the source due to scattering and absorption exclusively. This function is only defined for the transverse axis of the source, where $\theta_o = 90^\circ$ [8,9]. One can easily think of the radial dose function as a tissue attenuation correction factor, or more rigorously as an absorbed dose to kerma ratio in free space. The function is defined as:

$$g_L(r) = \frac{\dot{D}(r,\theta_o)}{\dot{D}(r_o,\theta_o)} \frac{G_L(r_o,\theta_o)}{G_L(r,\theta_o)}$$

Here $\frac{\dot{D}(r,\theta_o)}{\dot{D}(r_o,\theta_o)}$ is the ratio of the dose-rate at the distance of interest and ninety degrees to the dose-rate at one centimeter at the same angle. The ratio of the Geometric functions follows the same convention.

The Anisotropy is the angular variation in dose-rate at every angle around the source, for the same distance. This dose variation is due to the self-filtration within the source, oblique filtration of primary photons through the source encapsulation, and scattering of photons in the source medium[8,9]. It is defined as unity in the transverse plane for each distance measured, and given by:

$$F(r,\theta) = \frac{\dot{D}(r,\theta)}{\dot{D}(r,\theta_o)} \frac{G_L(r,\theta_o)}{G_L(r,\theta)}$$

1.5 MONTE CARLO PROCESS

The Monte Carlo process is an iterative computational method that utilizes aleatory techniques and numbers to examine and investigate the behavior of physical processes and mathematical systems. It is considered the "golden standard" method in studying a broad array of problems and cases where it is not possible or practical to compute an exact solution through deterministic algorithms – these include the particle transport and interactions of ionizing and non-ionizing radiation with different media[2].

The Monte Carlo method has proven to be a very useful statistical sampling computational technique in attaining approximate numerical solutions to systems and quantitative problems which are extremely complex, non-linear or involve significant uncertainties in inputs or have too large a number of coupled degrees of freedom to solve analytically. In these type of problems, Monte Carlo approaches are known to be the most accurate; yet widespread use of the techniques did not become ubiquitous until the last twenty years, when the increasing access to computers and computing power have made it practical[13].

The term Monte Carlo was originally coined during the 1940's by Stanislav Ulam and John von Neumann while working at the Los Alamos National Laboratory. The name makes reference to the use of random numbers and stochastic processes similar to those found in casino games, particularly the Monte Carlo Grand Casino located in the European principality of Monaco. The actual process was envisioned by Ulam while investigating neutron shielding with

various materials. Despite having most of the data necessary to perform the shielding calculations - atomic number of materials, mean-free path of the neutron and average energy transfer per collision - the calculations proved to be too cumbersome for analytical solutions. Instead simulations were developed with the use of random numbers to obtain a numerical solution to the neutron shielding problem[14].

We seek to give a more in-depth discussion of the Monte Carlo process. To do this, we find that the theory of branching processes become quite convenient – for us this means following the development of a large number of photons, with distinct energy spectrums, as they scatter, absorb or escape from our region of interest, namely a virtual phantom. At each stage in these bifurcating processes a decision must be made based on statistical probabilities appropriate to the physical and geometric factors.[14,15] These probabilistic decisions begin at time $t = 0$, when the particle is "born," and we associate it with a spatial location and energy. The decisions following the birth of the particle include: the position of the subsequent interactions, the nature of those interactions –whether more photons will be created, the momentum that will be allocated at each step and the direction of propagation after the interaction. These statistical decisions will be made by the use of random or pseudo-random numbers. If a new medium is encountered, then the characteristics of this new medium are taken into account - atomic and mass number, density, electron density and most importantly mass-stopping power - and a detailed "tracking

history" of the particle is recorded. This process is then repeated until a statistically valid record is created.

The statistical validity of the Monte Carlo method is provided by The Law of Large Numbers. We see that if performed enough times, the expectation value of the distribution obtained by the simulation, *f(x)*, process will approach the true distribution value. That is:

$$\lim_{N\to\infty} \frac{1}{N}\sum_{n=1}^{N} f(x_n) = \mathrm{I}$$

Where *I* is the real value of the distribution. In order to estimate the error in the simulation we need to introduce the variance of the estimated function:

$$\sigma^2(f) = (f(x) - \mathrm{I})^2$$

Now it can now be shown that:

$$\left(\lim_{N\to\infty} \frac{1}{N}\sum_{n=1}^{N} f(x_n) - \mathrm{I}\right)^2 = \frac{\sigma^2(f)}{N}$$

And employing The Central Limit Theorem, we can show that the Monte Carlo estimate bounded inferiorly by $-a$ and bounded superiorly by b, lies between:

$$\mathrm{I} - a\sigma(f)/\sqrt{N} \qquad \text{And} \qquad \mathrm{I} + b\sigma(f)/\sqrt{N}$$

As given by:

$$\lim_{N\to\infty} \Pr ob\left(-a\frac{\sigma(f)}{\sqrt{N}} \le \frac{1}{N}\sum_{n=1}^{N} f(x_n) - \mathrm{I} \le b\frac{\sigma(f)}{\sqrt{N}} \right) = \frac{1}{\sqrt{2\pi}}\int_{-a}^{b} dt\, e^{\left(\frac{t^2}{2}\right)}$$

Thus showing that the error in the Monte Carlo simulation scales as $\frac{1}{\sqrt{N}}$ [13,15].

This slow convergence dictates that a large number of events must be simulated in order to achieve a statistically valid record; for the purpose of this study 10^7 to 10^9 events were utilized.[15]

Having described the general process of the Monte Carlo method and justified its statistical validity, we now ask ourselves: How are the various decisions made? Random number generators are the core of the Monte Carlo process, and how the statistical decisions are determined. To start with, the random numbers must be generated with a uniform probability distribution – the use of pseudo-random numbers is common practice due to the relative simplicity and availability of pseudo-random number generators versus the complexity and computing power needed for generating truly random numbers. Once an algorithm for generating uniformly distributed random numbers is obtained, these numbers must be transformed to describe the non-uniform distributions, *F* of the physical characteristic or interaction we are aiming to describe. If *T* is the function needed to achieve this transformation, then it can be shown that:

$$T = F^{-1}$$

For example, it is known that the intensity of mono-energetic photons in a homogeneous material decreases exponentially with distance traveled in the material:

$$I = I_0 \, e^{-\mu_m x}$$

So in the interval $(0,\infty)$, if x is uniformly distributed in the open interval $(0,1)$, then:

$$T = -\ln(x)$$

Will give a non-uniform distribution of F with exactly those properties.[15] Now we have a method of applying the random numbers to the various statistical processes in order to simulate all particles.

1.6 MCNP5 CODE

MCNP is a general-purpose Monte Carlo N–Particle code that can be used for neutron, photon, electron, or coupled neutron and photon and electron transport. The code treats an arbitrary three-dimensional configuration of materials in geometric volume cells bounded by geometric surfaces of all types. Cross-section data are regularly updated and a point-wise cross-section data method is used. For photons, the code accounts for incoherent, coherent scattering, photo-electric events and photo-nuclear interactions. This includes the possibility of fluorescent emission after photoelectric absorption, and absorption in pair production with local emission of annihilation radiation, as well as

bremsstrahlung. In the case of electrons, a continuous-slowing-down model (R_{csda}) is used for electron transport which accounts for positrons, K-shell x-rays, and bremsstrahlung, but does not include external or self-induced fields. An important standard feature that makes MCNP very versatile and easy to use is a rich collection of variance reduction techniques, a flexible tally structure; and an extensive collection of cross-section data.[16]

1.6.1 INPUT FILE

The structure of the MCNP5 input file is defined by five sections – Cell Card, Surface Card, Source Definition Card, Material Card and Tallies Card. The Cell Card is the section where all the material densities, volumes or cells in the problem geometry are specified. The volumes are defined by the bounding surfaces within a Cartesian coordinate system and with the convention of using the minus sign, "-"to specify a volume that extends in the negative direction towards quadrants II and III. The cell volumes can be specified by the intersection, unions and complements of the regions bounded by the surfaces.

The Surface Card must follow the Cell Card and specifies all of the surfaces that create the problem geometry. MCNP5 is capable of creating first and second degree surfaces and fourth degree elliptical tori. The surfaces are specified by supplying coefficients to the analytic surface equations, or for certain types of surfaces, known points on the surface. The Source Definition Card defines the type of source that will be used, for our purpose we have defined an

isotropic cylindrical source that emits photons according to the specified energy spectrum, and accounts for secondary electrons. The energy spectrum is defined in terms of the energies of emitted photons with the corresponding emission probabilities. The Source Definition Card requires that one specifies where in the Cartesian system the source is located, what cell volume the location corresponds to, and the statistical importance associated with each cell in the problem geometry as well as any source biasing or statistical technique used to increase accuracy.

The Material Card allows the specification of the materials that will fill each geometric volume. Materials are specified by their elemental composition and the normalized mass fraction of each element. If a specific cross-section library is used it can be specified here after the definition of each element. The last Card in the MCNP5 input file consists of specifying what we want to measure. MCNP5 is capable of calculating a myriad of quantities. For the purpose of this Thesis the Point Detector, *F5 tally and Cell Heating, *F4, tally were used each yielding the energy deposited per area (MeV/cm^2).

1.6.2 POINT DETECTOR (*F5) Tally

The point detector, also known as the "next-event estimator" is an estimation of the flux, or charge deposition, at a point in space. It is commonly referred to as the "next-event estimator" because it tallies the flux at a point as if the last event were given by a particle trajectory directly to the detector without

further interactions, although contributions to the tally are made at source, and collision events throughout the particle's random walk. The result of the *F5 tally has units of MeV/cm^2. The physics justification of the point detector follows:

If we consider the point detector to be a sphere with a shrinking radius towards zero, and letting Ω_p be the direction to the center of the sphere, $d\Omega_p$ be the solid angle created by the detector sphere from **r**, and *dA* defined as the intersection of a plane passing through the detector point.

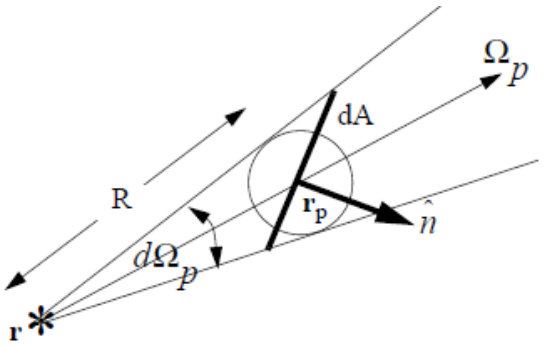

Figure 5: Graphical depiction of the contributions to the point detector tally, made at source and collision events throughout the random walk. The point detector is considered as a sphere whose radius is shrinking towards zero. Reproduced with permission from Forrest Brown, Ph.D., MCNP5/X Development Team Leader, Los Alamos National Laboratory.

For a particle to contribute to the flux once it passes *dA* it must fulfill two conditions: The particle must scatter into the solid angle $d\Omega_p$ towards *dA*, and it must have a flight free of collisions from the last event, **r**, to the sphere. These conditions occur with probabilities $p(\Omega_p)d\Omega_p$ and $e^{-\int_0^R -\Sigma_t(s)ds}$ respectively, with total probability $p(\Omega_p)d\Omega_p e^{-\int_0^R \Sigma_t(s)ds}$, where $\Sigma_t(s)$ is the total macroscopic cross-section at a distance *s* from the source collision point. If the interacting particle that reaches *dA* has a weight *w*, added to improve the Monte Carlo statistics, then it will contribute to the flux by an amount $\frac{w}{|\eta|dA}$, where η is the cosine of the angle between the particle direction and the normal to *dA*, $\eta = \Omega_p \cdot \hat{\mathbf{n}}$. As the detector sphere begins to shrink towards zero (a point), the angle subtended by *dA* becomes $d\Omega_p = {|\eta|dA}/{R^2}$, with the sides of the cone tending towards forming a cylinder and thus the tally (F5) becoming[16]:

$$F5 = p(\Omega_p)d\Omega_p \; e^{-\int_0^R -\Sigma_t(s)ds} \frac{w}{|\eta|dA} = w\frac{p(\Omega_p)}{R^2} e^{-\int_0^R -\Sigma_t(s)ds}$$

1.6.3 THE ENERGY FLUX DEPOSITION (*F4) DETECTOR TALLY

The *F4 Tally is an estimate of the average energy deposited by a photon, per unit area, in a specified cell. It is derived from the average photon flux in the

same cell and multiplied by flux to dose conversion factors specified by The National Council on Radiation Protection and Measurements (NCRP) and The American National Standards Institute (ANSI)[17] (Table I.). The mathematical explanation for the tally follows - the average particle flux in a cell can be written as,

$$\bar{\phi}_V = \frac{1}{V}\int dE \int dt \int dV \int d\Omega \, \Psi\left(\vec{r}, \hat{\Omega}, E, t\right)$$

$$= \frac{1}{V}\int dE \int dV \int d\Omega \int dt \quad \nu \, n\left(\vec{r}, \hat{\Omega}, E, t\right)$$

$$= \frac{1}{V}\int dE \int dV \int dt \quad \nu \, N\left(\vec{r}, E, t\right),$$

Where $N\left(\vec{r}, E, t\right) = \int d\Omega \, n\left(\vec{r}, \hat{\Omega}, E, t\right)$ is the density of particles at a point. Letting $ds = v\,dt$, ds being the differential track length we obtain a simplified equation for the flux $\bar{\phi}_V = \frac{1}{V}\int dE \int dV \int ds \, N\left(\vec{r}, E, t\right)$, where $N\left(\vec{r}, E, t\right)$ may be thought of as the track length density; this allows the flux to be estimated by a sum of the individual track lengths. The estimates of the flux are divided into separate time-dependent and energy-dependent estimates by binning the track lengths in the respective bins[16].

Table I: Conversion factors for energy deposited by photon flux (in *MeV)* to dose-rate (in *rem/hr)/(particle/cm^2-second)*[17]. Table data are used to calculate the Kerma strength in vacuum at 100 cm and dose-rate in water at 1cm in the transvers plane of the source. The Table is also used in the calculation of dose-rate to simulated organ tissues.

ANSI/ANS–6.1.1–1977			
Energy *MeV*	DF *(rem/hr)/(p/cm²-s)*	Energy *MeV*	DF *(rem/hr)/(p/cm2-s)*
0.01	3.96E–06	1	1.98E–06
0.03	5.82E–07	1.4	2.51E–06
0.05	2.90E–07	1.8	2.99E–06
0.07	2.58E–07	2.2	3.42E–06
0.1	2.83E–07	2.6	3.82E–06
0.15	3.79E–07	2.8	4.01E–06
0.2	5.01E–07	3.25	4.41E–06
0.25	6.31E–07	3.75	4.83E–06
0.3	7.59E–07	4.25	5.23E–06
0.35	8.78E–07	4.75	5.60E–06
0.4	9.85E–07	5	5.80E–06
0.45	1.08E–06	5.25	6.01E–06
0.5	1.17E–06	5.75	6.37E–06
0.55	1.27E–06	6.25	6.74E–06
0.6	1.36E–06		
0.65	1.44E–06		
0.7	1.52E–06		
0.8	1.68E–06		

The reliability of the track length estimator is quite good, since there are usually many tracks entering a particular cell, versus respectively fewer collisions, leading an abundance of individual contributions[16].

1.6.4 Ir^{192} SOURCE

The Nucletron source model No. 105.002 was selected because it is one of the most widely utilized HDR sources worldwide. The dimensions of the Nucletron® Ir^{192} source were obtained from the manufacturer's specifications for the Food and Drug Administration (FDA) 510K filings through the publication of *Daskalov et al.*[18] The source consists of a pure Ir^{192} metal cylinder (density of 22.42 g cm^{-3} and half life of 73.827 days), of diameter 0.65 mm and length 3.6 mm, throughout which the radioactive Iridium is homogeneously distributed. It has rounded edges (thickness 0.20 mm) allowing more ease of movement through curved catheters. The radioactive source is encapsulated in a hollow cylinder of ANSI 316L steel of 4.5 mm in length and 0.9 mm in diameter (density 8.02 g cm^{-3} and composition by weight of 2% Mn, 1% Si, 17% Cr, 12% Ni and 68% Fe (Table. II.). The source is attached to a stainless steel cable of 200 mm length and 0.7 mm diameter (Figure 6.).

Table II: Elemental composition of ANSI 316L steel used in the source encapsulation and source driving cable.

Element	% Mass Fraction	Element	% Mass Fraction
Fe	66.5	Si	1.0
Cr	17.0	Mo	2.5
Ni	12.0	Rh	1.0

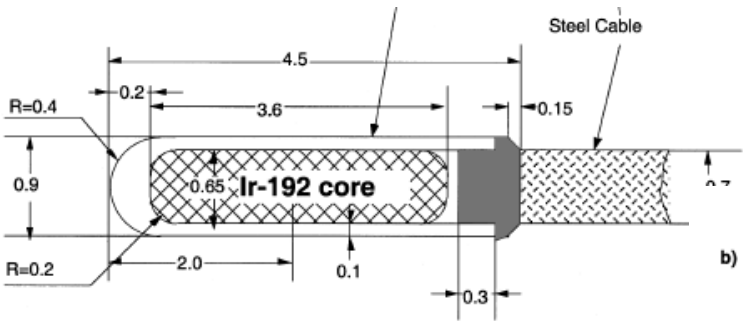

Figure 6: Geometry for the Nucletron Ir^{192} HDR brachytherapy source modeled in the Monte Carlo simulation (all dimensions are in millimiters). Image has been reproduced with permission from the AAPM.

1.6.5 Ir^{192} ENERGY SPECTRUM

An updated energy spectrum for Iridium-192 was obtained from the publication by M. J. Rivard *et al*[19] and confirmed with the data from The National Institute of Standard and Technology (NIST) and The National Nuclear Data Center (NuDAT.) In past studies of Ir^{192} brachytherapy sources no single spectrum has been defined, but rather five different spectra have been used. The spectrum utilized in this Monte Carlo simulation completely accounts for the influence of 70*KeV* photons that were excluded in previous works. This spectrum, when used in the simulations, yields an average energy of 371.0 *KeV*.

Table III: Photon energy spectra for Ir^{192} from investigations by Glasgow and Dillman, the Amersham Medical Radiation Sources Catalogue, Shirley, Duchemin and Coursol, and NNDC. Image has been reproduced with the permission of Mark J. Rivard.

Glasgow & Dillman		Amersham		Shirley		Duchemin & Coursol		NNDC	
Energy (keV)	Intensity (photons/Bq)	Energy (keV)	Intensity (photons/Bq)	Energy (keV)	Intensity (photons/Bq)	Energy (keV)	Intensity (photons/Bq)	Energy (keV)	Intensity (photons/Bq)
7.82	0.000119								
8.27	0.00000652								
8.84	0.000712								
8.91	0.00638							8.91	0.0153
9.34	0.0000952								
9.36	0.00173								
9.44	0.0155							9.44	0.0396
9.98	0.000287								
10.18	0.000383								
10.22	0.0000874								
10.35	0.00449								
10.51	0.000523					7-14	0.058		
10.60	0.00149								
10.84	0.000222								
10.85	0.000516								
10.87	0.0000842								
11.07	0.0132								
11.23	0.000675								
11.25	0.00372								
11.56	0.000307								
12.10	0.000868								
12.38	0.0000741								
12.42	0.000120								
12.50	0.000172								
12.94	0.00260								
13.27	0.000481								
13.36	0.000228								
60.90	0.0000112								
61.49	0.0127			61.49	0.016			61.486	0.0120
63.00	0.0219			63.00	0.0203			63.0	0.0205
64.51	0.0000288					61-67	0.1072		
65.12	0.0267							65.122	0.0263
66.83	0.0458							66.831	0.0446
71.08	0.00252							71.079	0.00241
71.41	0.00487			71.30	0.006629			71.414	0.00466
71.88	0.000119								
73.44	0.00191			73.40	0.001732			73.363	0.00163
75.37	0.00540							75.368	0.00533
75.75	0.0103					71-79	0.02892	75.749	0.01025
76.24	0.000267								
77.92	0.00416							77.831	0.00365
110.09	0.00115			110.09	0.0001269			110.4	0.000122

1.7 PHOTON TRANSPORT IN MCNP5

MCNP5 has two models to simulate the photon transport: *Simple* and *Detailed.* The *Simple* model, as the name implies, is generally less accurate and mainly used for photons with energies in the *MeV* range. The model ignores coherent scattering (Thomson) and fluorescent photons arising from photo-electric absorption and hence is not used in this work.

The *Detailed* physics treatment was the method selected for all photon transport and includes Thomson scattering, fluorescent photons occurring after photo-electric absorption as well as incoherent scattering (Compton), Pair-production and photo-nuclear interactions – provided that the energies are sufficiently high for the last two types of interactions. The effects of electron binding are generally considered by the use of Form Factors for coherent and incoherent scattering. The possibility of secondary electron emission is considered for all photon interactions, except coherent scattering, and full electron transport is applied[16].

1.7.1 INCOHERENT (COMPTON) SCATTERING

When modeling incoherent scattering the angle of scattering from the incident line of flight, θ, the energy of the resulting scattered photon, E', and that of the recoil electron, $E - E'$ must all be determined. This yields the energy deposited at the point of collision and can be thus assumed to add to the dose in medium. Before these quantities of interest can be determined, the probability

that the event in question is in fact a Compton event must be calculated – the Compton cross-section has to be determined. The cross-section is obtained by a modification of the Klein- Nishina cross-section formula:

$$\sigma(z,\alpha,\mu)d\mu = I(z,\nu)\,K(\alpha,\mu)d\mu$$

Where *I(z,v)* is a factor that modifies the Klein-Nishina cross-section by decreasing its value, per electron, in the forward direction for low energy, E, and high atomic number, Z, independently, such that $I(Z,0)=0$ & $I(Z,\infty)=Z$.

$$K(\alpha,\mu)d\mu = \pi r^2\left(\frac{\alpha'}{\alpha}\right)^2\left[\frac{\alpha'}{\alpha}+\frac{\alpha}{\alpha'}+\mu^2-1\right]d\mu$$

Is the actual Klein-Nishina cross-section formula, with r_0 being the classical electron radius ($2.817938\text{x}10^{-13}$ *cm*), α and α' being the incident and final photon energies in units of electron rest mass, $\mu = cos(\theta)$, the cosine of the angle of deflection from the photon line of flight, and *v* is the inverse length[16].

1.7.1 PHOTO-ELECTRIC EFFECT

The photo-electric effect involves the absorption of an incident photon with energy *E*, with the subsequent emission of several fluorescent photons and the ejection or excitation of an orbital electron (binding energy $e < E$). This gives the ejected electron a kinetic energy of $E - e_b$. MCNP5 accounts for three flourescent emission cases**,** where zero, one or two photons are emitted[16].

1.7.2 COHERENT (THOMSON) SCATTERING

Thompson scattering does not change the energy of the incoming photon – has no energy loss – hence the only parameter that needs to be computed is θ, the scattering angle. The transport of the subsequent photon continues through the media in the usual manner[16].

2.0 MATERIALS AND METHODS

The dosimetric parameters of the source are calculated by Monte Carlo transport methods utilizing the Monte Carlo N-Particle 5 (MCNP5) software, and include only the contribution of photons. The influence of β- particles (electrons) is assumed negligible, as suggested by the work of *Medich et al.*[20], due to the filtration that occurs in the source encapsulation[20,21]. The dose data, anisotropy, geometric and radial dose functions obtained via calculations through MCNP5 will be verified by comparison with results published by the American Association of Physicist in Medicine's (AAPM) Task Group 43 (TG-43) and current peer reviewed literature to validate the model.[8,9,10]

Because this work entails a computer simulation of a brachytherapy source, without *in vivo* verification, no clinical experiment was performed. Rather the Monte Carlo N-Particle 5 (MCNP5) software package - distributed by the Los Alamos National Laboratory - was used. Currently, methods of Monte Carlo are the golden standard for dosimetric investigations. The geometry for the Nucletron HDR source model No. 105.002 was obtained from the paper published by *Daskalov, et al.*[18], and the model was verified against results from that same publication, the results presented by *Granero, et al.*[22] and the AAPM Task Group-

43, Update 1[2]. Verification of the geometric accuracy of the simulated source was accomplished by visualization with MCNP5's VisEd 5-4.23. The input file was created and executed on a Dell Inspiron 15 computer with an Intel® Core™ i5 processor, 64 bit operating system, running at 2.3GHz with 4.00 GB of RAM, in a Windows® platform.

2.1 Ir^{192} SOURCE MODEL

The geometry of the problem was modeled in a manner similar to the accepted peer reviewed publications (Figure 7.). A homogenous cylindrical Ir^{192} source was placed at the center of the problem geometry, $(x = 0, y = 0, z = 0)$ and expanded in the positive and negative $\hat{x}$ directions by 1.8 mm, creating a total length of 3.6 mm; the cylinder was given a radius of 0.325 mm. The source encapsulation was modeled with ANSI 316L Stainless Steel by creating a hollow cylinder with external radius of 0.45 mm and an internal radius of 0.325 mm, making it tight against the Ir^{192} core. The distal end of the encapsulation, $+\hat{x}$, was modeled with a hemisphere of radius 0.059 mm and the end proximal to the cable was modeled with a solid, Stainless Steel cylinder of radius equal to the Ir^{192} core and attached to a cone opening in the $-\hat{x}$ direction. The woven steel cable is assumed to be made of the same material as the source encapsulation and is modeled as a solid cylinder of radius 0.35 mm with a length of one centimeter.

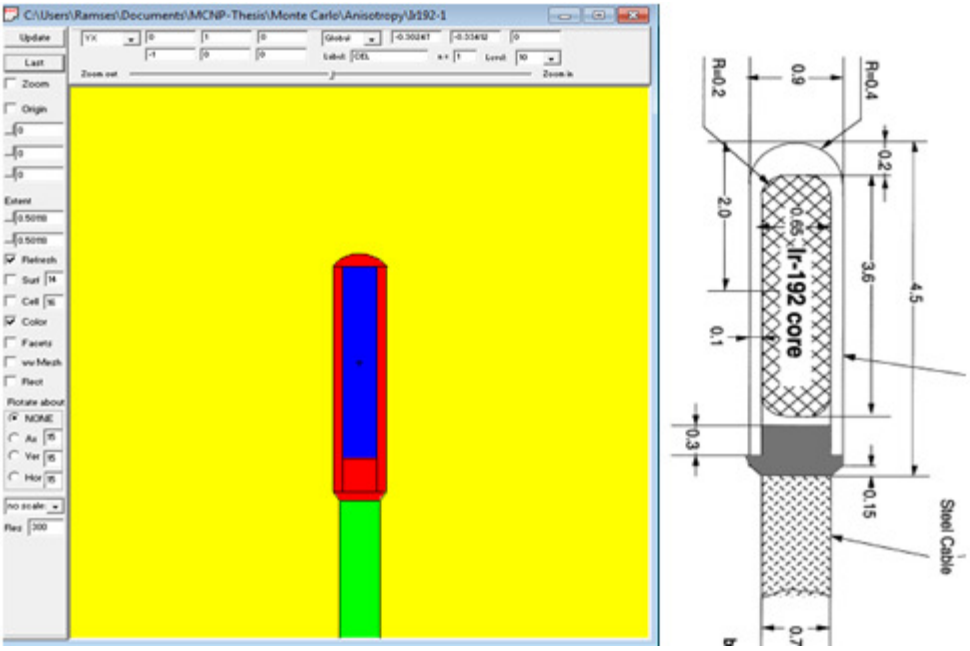

Figure 7: VisEd depiction of the Ir^{192} HDR Source (left) and geometry reported by Daskalov *et al.*[18] Each color represents a distinct material - blue is iridium, red is ANSI 316L Steel, green is the woven steel cable – assumed same as encapsulation, and yellow is water. Dimensions are in millimiters.

2.2 PHANTOM MODEL

The entire source is embedded at the center of a spherical phantom of 20 cm in radius. The materials that fill the phantom vary between water (density 1g cm^{-3}), dry air (density 0.00119 g cm^{-3}) and vacuum (density 0.0 g cm^{-3}) depending on the parameter being investigated. The vacuum and air filled phantom is explicitly in the simulation for measuring the Air-Kerma Strength, S_K, at a distance of 100 cm from the source in the transverse plane, while the water filled

model is used for all other calculations. Point Detectors, *F5, and Cell Heating tallies, *F4, were used to score the doses.

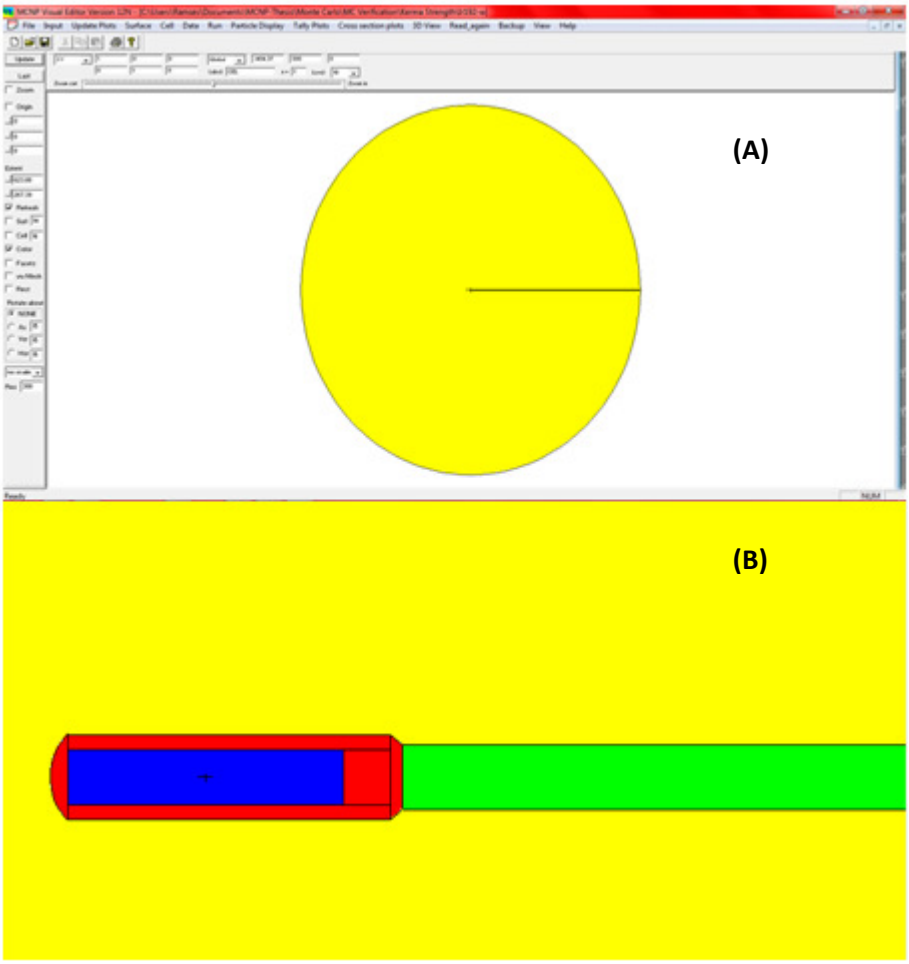

Figure 8: VisEd visualization of the: (A) virtual water-filled spherical phantom with a diameter of 40 cm, and (B) The simulated Ir^{192} HDR brachytherapy source at the phantom center, with encapsulation and steel driving cable.

2.3 MODEL VERIFICATION

The model was tested under the conditions dictated by TG-43[9,10], Daskalov *et al*[18], and Granero *et al.*[22] All the dosimetric parameters of TG-43 were calculated and verified against the literature, with accepted results having a Monte Carlo uncertainty ≤ 1% and a total difference from published results ≤ 2%.

2.3.1 GEOMETRIC FUNCTION VERIFICATION

The purpose of the Geometric function is to provide a corrected approximation of the dose fall off with distance – to properly account for the effect of the spatial arrangement of the radioactive material on dose distribution. If the spatial extent of the source were negligible, an inverse square approximation would yield sufficiently correct results. For a linear source with finite length the Geometric function is: $G_L = \begin{cases} \dfrac{\beta}{L r \sin\theta} & , \theta \neq 0^\circ \end{cases}$

Where β is the angle subtended by the source end-points and the point of dose measurement (Figure.4). Calculation of the angle β and the Geometric function is not trivial; the reader is referred to the publication by R. P. King *et al*[23] for a detailed derivation. The angle β and the Geometric function are calculated from the following formulas:

$$\beta = \sin^{-1}\left(\frac{\sin\left(\tan^{-1}\left[\frac{[r\sin(\theta)]}{r\cos(\theta)-L/2}\right]\right)}{\sqrt{[r\sin(\theta)]^2+\left[r\cos(\theta)+L/2\right]^2}}\right)$$

$$G_L = \frac{\sin^{-1}\left(\frac{\sin\left(\tan^{-1}\left[\frac{[r\sin(\theta)]}{r\cos(\theta)-L/2}\right]\right)}{\sqrt{[r\sin(\theta)]^2+\left[r\cos(\theta)+L/2\right]^2}}\right)}{L\,r\sin(\theta)}$$

Here *r* is the distance from the center of source's radioactive distribution to the point of measurement. The angle θ, is the angle subtended by a line from the source center to the point of measurement and *L* is the length of the source's radioactive distribution (Figure 4.).

2.3.2 ANISOTROPY FUNCTION VERIFICATION

The Anisotropy function *F(r,θ)*, provides a measure of the dose variation as a function of polar angle around the source, for a given distance. Simulated measurements were made in the water phantom of 20 cm radius by placing point detectors (*F5) at several angles that could be easily compared with the published literature, and at distances of one, two, three and five centimeters from the source center. For the purpose of the anisotropy function, and to exclude the influence of

secondary electrons caused by the interactions of primary photons with the source cable, we define the zero degrees as the distal end of the source.

The anisotropy function is obtained from the ratio of the dose-rate at the distance of measurement, *r*, and angle of measurement with respect to the horizontal θ, and the dose-rate at the same distance *r*, and at the angle of the transverse plane θ_o (ninety degrees) multiplied by a similar and inversed ratio of the Geometric function. The results from the *F5 detector tally did not need to be converted to the standard units of dose-rate since the result from each angle is normalized by the result at 90 degrees, hence cancelling out any multiplicative factor.

$$F(r,\theta)=\frac{\dot{D}(r,\theta)}{\dot{D}(r,\theta_o)}\,\frac{G_L(r,\theta_o)}{G_L(r,\theta)}$$

2.3.3 RADIAL DOSE FUNCTION VERIFICATION

The effect of the radial dose function is to correct for the attenuation or absorption and scattering through the material which the photon transport takes place. It is calculated from the ratio of the dose-rate at a distance of interest, *r*, in the transverse plane of the source ($\theta_0 = 90°$) to the dose-rate at a distance of one centimeter in the same plane, all multiplied by a similar and inversed ratio of the geometric function.

$$g_L(r)=\frac{\dot{D}(r,\theta_o)}{\dot{D}(r_o,\theta_o)}\frac{G_L(r_o,\theta_o)}{G_L(r,\theta_o)}$$

To achieve the desirable level of comparison with the literature, the distances investigated were 1.5 cm, and from one to ten centimeters, in one centimeter intervals. Point detector (*F5) tallies were placed at the indicated distances and the simulation was run for 10^7 histories. Similarly to the case for the Anisotropy Function, the results at each distance for the Radial Dose Function did not need to be converted to customary units for dose-rate because they are normalized by the result at 1 cm, hence cancelling any multiplicative factor.

2.3.4 DOSE-RATE CONSTANT VERIFICATION

The dose-rate constant was obtained by the method specified in the AAPM Task Group 43[8,9]. The dose-rate constant is calculated by:

$$\Lambda=\frac{\dot{D}(r=1cm,\theta=90°)}{S_K(r=100cm,\theta=90°)}$$

Where $\dot{D}(r=1cm,\theta=90°)$ is the dose-rate at one centimeter from the source center along the transverse bisector plane in a homogeneous medium of water, and $S_K(r=100cm,\theta=90°)$ is the Air-Kerma strength of the source measured at 100 cm from the source center along the same plane, but without the influence of scattering or absorption in the medium.

2.3.4.1 AIR-KERMA STRENGTH MEASUREMENT

The Kerma strength of the source was measured by placing a small sphere, with volume of 1 mm^3, filled with dry air at a distance of 1 m from the transverse plane of the source. The source was placed at the center of a spherical phantom that was expanded to a diameter of 5 m and filled with *vacuo* material. The Ir^{192} HDR source model used in the verification of the anisotropy, geometric and radial dose function was also used here. Placing a small sphere with air at the point where the air-Kerma strength is being measured fulfills the requirement that the Kerma strength be measured to a mass of air in which the photons have not previously undergone any scattering or absorption. This method offers a lower level of uncertainty when compared to previously used techniques that involve measurement of the Kerma strength in an air-filled phantom and latter implementing a $1/r^2$ attenuation correction for air.

The Kerma strength was scored using the *F4 track-length tally (MeV/cm^2) with the results separated into *1 KeV* bins using MCNP5's Dose-Energy (*DE*) card. The binned tally outputs were multiplied by the respective mass-energy absorption coefficients for dry air[20,24] μ_{en}/ρ. The mass-energy absorption coefficients were obtained from NIST and multiplied to the tally output via a look-up Table in Excel. The results were then multiplied by the Iridium-192 photon yield, $I_\gamma = 2.3541\ (\gamma\ Bq^{-1}\ s^{-1})$ and a conversion factor of 1 $MeV\ g^{-1}\ Bq^{-1}\ s^{-1} = 2.13x10^3\ cGy\ mCi^{-1}\ h^{-}\ MeV^{-1}\ g\ Bq\ \ s^{1}$ to bring the result to more familiar units. The result yielding the Kerma strength:

$$\dot{K}_{\delta}(r,\theta) = R_{TALLY}(r,\theta) \times \mu_{en}/\rho \times I_{\gamma} \left(2.13 \times 10^{3}\right) \left[\frac{cGy}{mCi\ h}\right] \quad 19$$

The Air-Kerma strength is obtained by multiplying the Kerma strength by the squared distance to the measuring point, 1 m, thus yielding the same numerical result with units of $\left[\frac{cGy\ m^2}{mCi\ h}\right]$.

Table IV: Elemental %-mass composition of dry air.

Element	%-Mass Fraction
C	0.012
N	75.59
O	23.2
Ar	1.2

2.3.4.2 DOSE-RATE AT 1 cm IN WATER

The dose rate was measured at a distance of one centimeter from the center of the source's radioactive distribution along the transverse bisector. The measurement was performed in the same simulated spherical phantom of 40 centimeters in diameter used for the verification of the other dosimetric parameters, except S_K. The dose was scored in a small, water-filled, sphere with a volume of one millimeter cubed centered at one centimeter from the source. Like

in the measurement of the Air-Kerma strength, the *F4 tally was used and the same approach to determining the dose-rate was also applied here. The data for the mass-energy absorption coefficient for liquid water was obtained from NIST and the same lookup table technique used in the kerma-strength calculation was used here. The photon yield and conversion factor utilized previously were also used to obtain an absorbed

dose rate of $\dot{D}(r = 1cm, \theta = 90°) = 2.56 \times 10^{7} \quad \left[\frac{cGy}{mCi\ h}\right]$.

Table V: Elemental %-mass composition of liquid water used in the Monte Carlo simulation.

Element	%-Mass Fraction
H	88.8
O	11.2

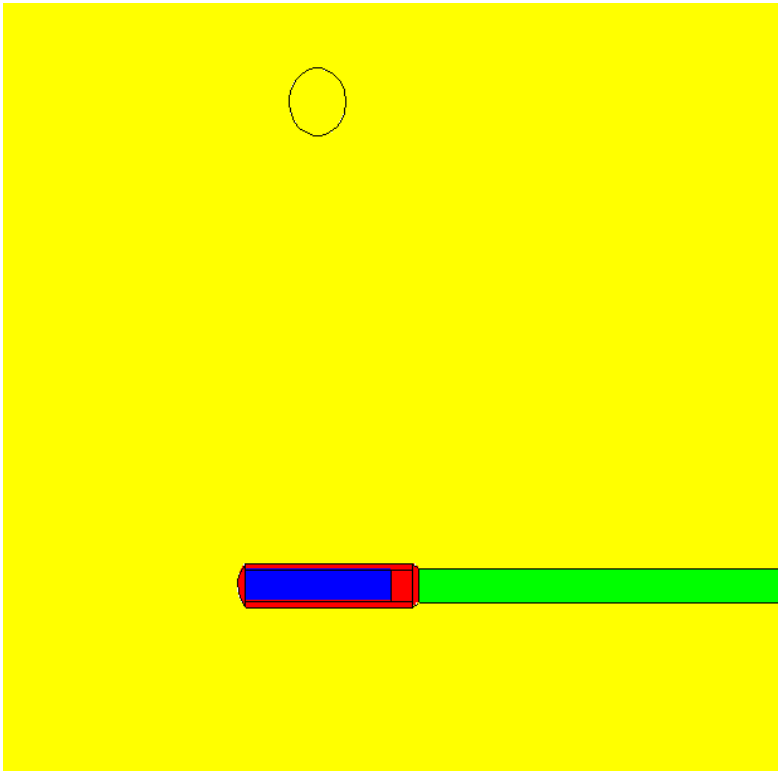

Figure 9: Close up of the Ir^{192} HDR source with encapsulation and steel cable in water phantom and a 1 mm^3 sphere at a distance of 1 cm from the center of the transverse plane of the source used for measuring the dose-rate.

2.4 INTRODUCTION OF HETEROGENEITIES

In order to more realistically measure the influence of organ heterogeneities in clinical dose calculations, it was decided to alter the phantom used in the model verification process to be more anthropomorphically correct. This was achieved by introducing approximations for a malignant prostate gland, a full bladder with urine and a rectum filled with air, into the spherical water-

filled phantom; the 40 cm diameter was kept since it allows for full backscatter conditions at each of the simulated organ heterogeneities. Each of the simulated organs was given their corresponding tissue densities(s) and elemental composition as normalized mass fractions, per specification in ICRU Report 47.[26]

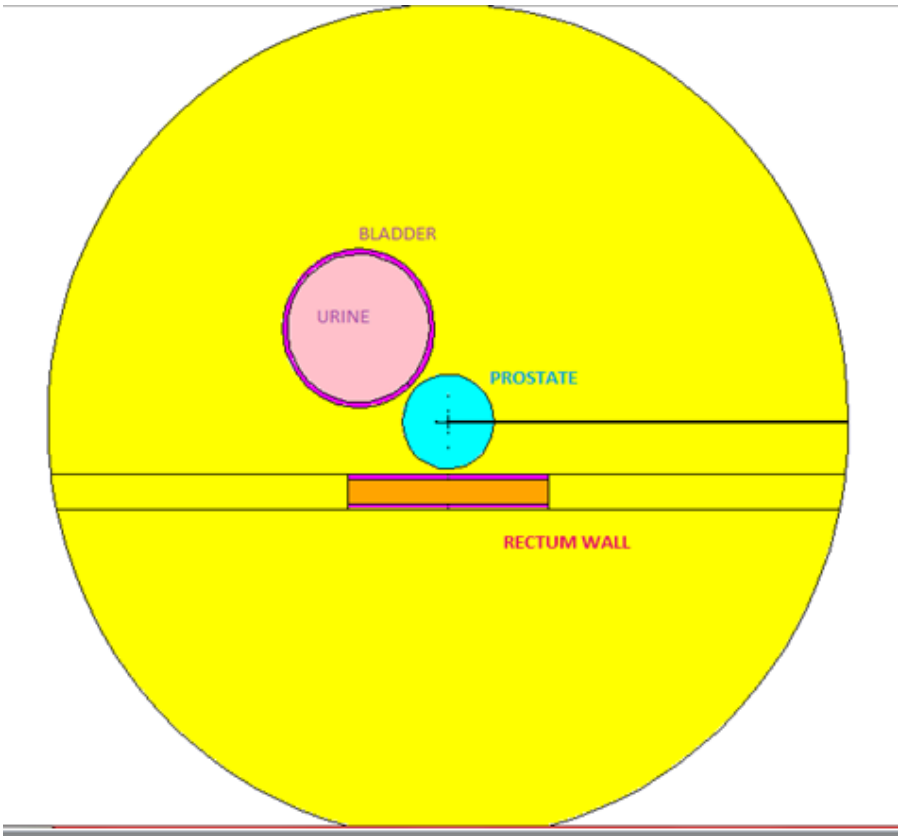

Figure 10: VisEd rendered visualization of the simulated phantom with the Ir^{192} HDR brachytherapy source in center and organ heterogeneities from prostate (aqua), bladder (dark pink), urine (light pink), rectum wall (dark pink) and air inside the rectum (brown).

2.4.1 PROSTATE

A malignant prostate was simulated at the center of the phantom, and surrounding the Ir^{192} source, by a sphere of radius 2.12 cm – a volume of 40 cm^3 as suggested by *Carrier and Beaulieu et a.l*[25] The prostate tissue composition was also obtained from the work by *Carrier and Beaulieu et al*. It is assumed that the prostate consists of homogeneous tissue. The dose inside the prostate was measured inside spheres of the same material with a volume of 1 mm^3, at seven locations. On the upper side of the source, $+\hat{y}$, along the transverce bisector, at distances of 0.5 cm, 1 cm and 2.0 cm; these measuring points were reflected along the long axis of the source, such that there are now in the $-\hat{y}$. A final measurement is made at 1 cm from the distal tip of the source by the same type of sphere.

Table VI: Prostate elemental %-mass composition.

Element	%-Mass Fraction	Element	%-Mass Fraction
Ca	0.023	O	78.1
C	9.11	P	0.10
H	9.76	K	0.20
Mg	0.019	Na	0.21
N	2.47	Zn	0.008

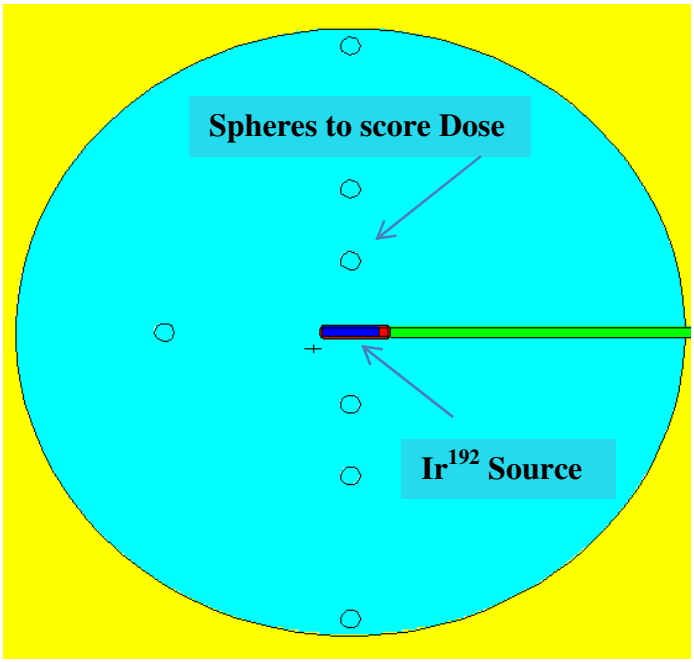

Figure 11: Virtual Prostate inside a simulated water phantom with Ir^{192} HDR brachytherapy source in the center and dose measurement spheres of 1 mm^3 at distances of 0.5, 1 and 2.0 cm on both sides of the source axis and at 1 cm from the distal tip of the source.

2.4.2 BLADDER

A full bladder was simulated by creating the bladder wall – 5 mm thick - from two concentric spheres, at a distance of 6.98 cm from the source center along the 45° diagonal, with radii of 4.273 cm and 3.773 cm respectively. The material filling the volume between the concentric spheres was defined as soft tissue, per the nine element definition in ICRU-47[26]. The inner volume of the

bladder was filled with urea (225 cm^3). The dose is measured in spheres with volume of 1 mm^3 placed in the outermost and innermost walls near the Iridium source and at the midpoint between the far inner and outer walls (Figure 12.).

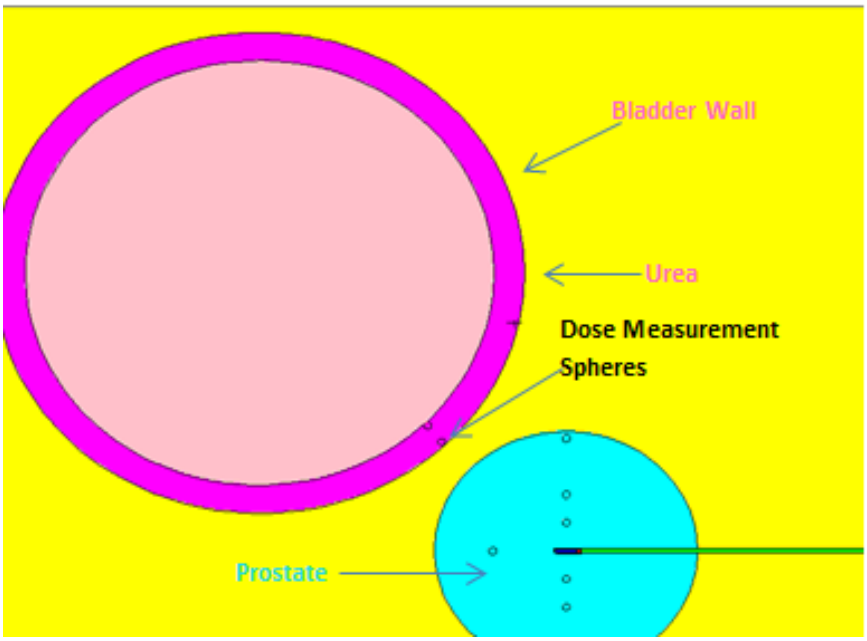

Figure 12: Simulated bladder with inner volume of 225 cm^3 filled with urea. The bladder wall has been defined as soft tissue. Spheres with volume of 1 mm^3 are placed in the near inner and outer bladder wall and in the inner far bladder wall for dose scoring.

Table VII: Elemental %-mass composition of soft tissue used as bladder wall and rectal wall.

Element	%-Mass Fraction	Element	%-Mass Fraction	Element	%-Mass Fraction
H	10.2	C	14.3	N	3.4
O	70.8	Na	0.2	P	0.3
S	0.3	Cl	0.2	K	0.3

Table VIII: Elemental %-mass composition of Urea.

Element	%-Mass Fraction
Mg	19.99
H	6.70
N	46.66
O	26.65

2.4.3 RECTUM

Creation of a virtual rectum inside the spherical phantom was accomplished by inserting two concentric cylinders with radii of 1.655 cm and 1.155 cm respectively. The cylinders are given a length of 18 cm, 9 cm along each direction of the X axis and displaced a distance of 5 cm from the prostate on

the Y axis. The data for the average rectal length and volume in males is provided in the work by *Hae Ran Yun, et al.*[27]. The volume between the concentric cylinders is filled with soft tissue (Table VII.) and the volume of the inner cylinder is filled with dry air in order to accurately describe the material inside an empty rectal canal (Figure 13.) Similarly to how the dose is scored in the bladder, $1mm^3$ spheres are placed at both, the rectal walls closest to the source (near walls) and furthers from the source (far wall), and at each of the inner and outer walls.

2.5 UNCERTAINTY ANALYSIS

Task Group 43 of the AAPM delineates a method for a rigorous uncertainty analysis that is based on the Technical Note 1297 from NIST, on the estimation of total uncertainty in Monte Carlo brachytherapy simulations[9]. These guidelines demand that analysis be done for the uncertainty in Monte Carlo Dose-Rate Constant, Λ_{MC}, Monte Carlo Radial Dose Function $g(r)_{MC}$, and absolute doses measured in the transverse plane.

The statistical method recommended by NIST involves the use of the Law of Propagation of Uncertainty (LPU.) This estimates the uncertainty in a quantity y, which changes with measured or estimated values of x_n, as follows:

$$y = f(x_1, ..., x_n),$$

$$\sigma_y^2 = \sum_{i=1}^{N} \left(\frac{\partial f}{\partial x_i} \right) \sigma_{x_i}^2 + 2 \sum_{i=1}^{N-1} \sum_{j=i+1}^{N} \frac{\partial f}{\partial x_i} \frac{\partial f}{\partial x_j} \sigma_{x_i x_j}$$

Where the covariance of the two variables, $\sigma_{x_i x_j}$, is assumed to be zero. The uncertainty of each dosimetric parameter in brachytherapy simulations is composed of three causes: (1) The uncertainty of the underlying cross-sections, σ_μ, (2) the uncertainty associated with the source geometry, σ_{geo}, and (3) the uncertainty intrinsic to the Monte Carlo simulation itself, σ_{MC}. These three causes of uncertainty transform the LPU equation into:

$$\%\sigma_Y = \sqrt{\%\sigma_\mu^2 + \%\sigma_{geo}^2 + \%\sigma_{MC}^2}$$

$$\equiv \sqrt{\left(\%\frac{\partial Y}{\partial \mu} \right)^2 \%\sigma_\mu^2 + \left(\%\frac{\partial Y}{\partial geo} \right)^2 \%\sigma_{geo}^2 + \%\sigma_{MC}^2}$$

The uncertainties associated with the simulated geometry have not been studied in much depth. This is mainly due to poor understanding of the unique and numerous geometric parameters that make up the simulation, and the level of complexity involved in analyzing their correlated probability distributions. For these reasons the geometric uncertainty is not calculated in this work.

The uncertainty associated with the Monte Carlo simulation, g_{MC}, is composed of the intrinsic uncertainty associated with Monte Carlo simulations, as

well as the uncertainty associated with energy spectrum and the photon yield of the source, $g_{I\gamma}$.

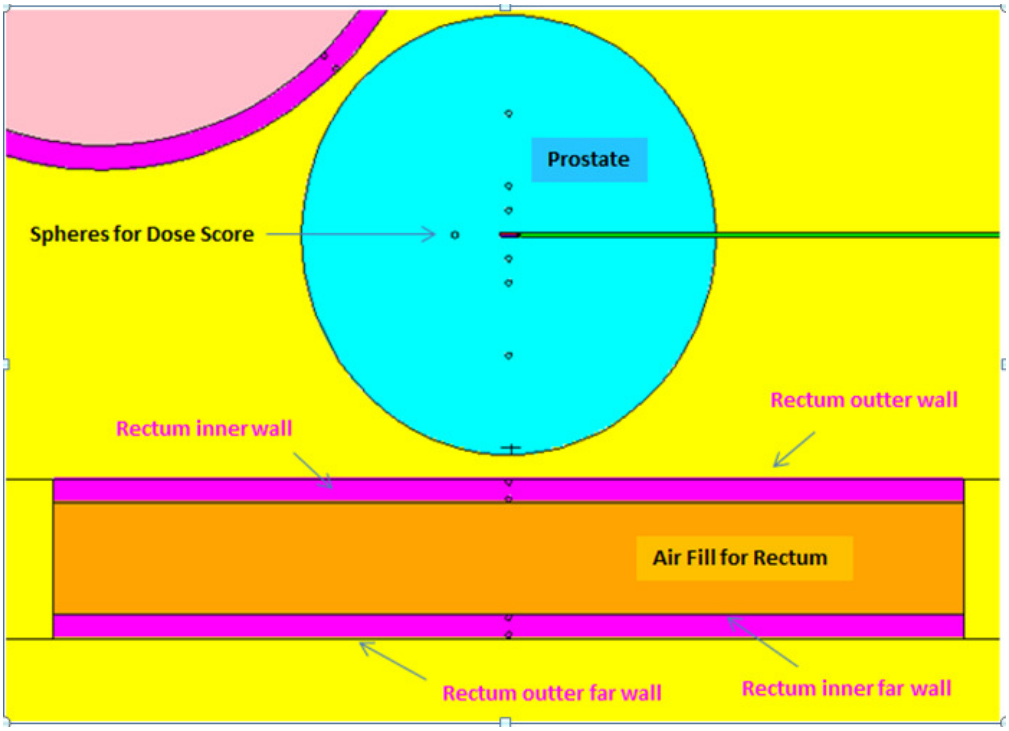

Figure 13: Simulated rectum with 5 mm thick wall and inner air filled volume of 6.45 cm^3, inside virtual phantom. The rectum wall has been defined as soft tissue. Spheres with volume of 1 mm^3 are placed in the near inner and outer rectal walls and in the inner and outer far rectal wall, for dose scoring.

3.0 RESULTS AND DISCUSSION

3.1 ANISOTROPY AND GEOMETRIC FUNCTIONS

The Monte Carlo simulation for Anisotropy yielded results that compare well with the data provided by *Daskalov et al*[18]. The Anisotropy results of the Monte Carlo were allowed to differ by up to four percent from those of *Daskalov et al.* This discrepancy is justified because data for exact angles were not provided in the referenced publications – on a similar note, comparison with data from TG-43[8] are not deemed relevant for the Anisotropy function because the data provided in this report are for permanent seed implants, not HDR sources. The maximum discrepancy between the computed results and the established data was 3.6% and 4% at two and three centimeters from the source center, respectively, and at an angle of two degrees. This difference is well within the acceptable statistical variability, thus there was no need to implement statistical enhancement techniques.

The uncertainty associated with the Anisotropy Function $F(r,\theta)$ at each distance varied from 2.9% at 1 cm to 3.7% at 5 cm (Table IX.), and was calculated from the equation below:

$$\sigma_F(r,\theta) = F(r,\theta)\sqrt{\sigma_{MC}(r,\theta)^2 + \sigma_{MC}(r_0,\theta_0)^2 + 2(\sigma_\mu)^2}$$

Table IX: Uncetainty for the Anisotropy Function at each calculated distance *r*.

Anisotropy Uncertainty	
distance *(cm)*	Uncertainty (σ_F)
1	2.92%
2	3.29%
3	3.35%
5	3.70%

Tables X through XIII below show the values of the calculated Geometric Function, including the angle β, the Monte Carlo calculated Anisotropy Function values, the Anisotropy Function values provided by *Daskalov et al*[18]., and the relative percent difference of the Monte Carlo calculated values for the Anisotropy Function versus the published values for distances of one to five centimeters from the source center. Similarly, Figures fourteen through seventeen show the plotted graph of the Monte Carlo calculated values for the Anisotropy Function from one to five centimeters from the source center, and for polar angles from zero to 90°, compared to the results obtained by *Daskalov et al.*[18]

Table X: Monte Carlo simulation results for the Anisotropy Function $F(r,\theta)$ at 1 cm from the source center and compared to results from *Daskalov et al*[18]. Results for the angle β and the Geometric function are also provided.

Anisotropy Function r=1 cm						
Monte Carlo Results					Daskalov *et al*	% Difference
Angle θ (degrees)	β	G_0	G_L	Anisotropy F(r,θ)	Anisotropy F(r,θ)	
2	0.36286	14.28546	14.4407	0.67531	0.6520	3.6%
6	1.08670		14.4392	0.70969	0.6960	2.0%
10	1.80490		14.4361	0.74400	0.7450	-0.1%
16	0.78990		14.4289	0.78990	0.8120	-2.7%
20	0.86582		14.4224	0.86582	0.8460	2.3%
26	0.92611		14.4106	0.92611	0.8990	3.0%
30	0.90060		14.4015	0.90060	0.9290	-3.1%
36	0.91914		14.3865	0.91914	0.9290	-1.1%
40	0.94308		14.3759	0.94308	0.9450	-0.2%
46	0.95214		14.3597	0.95214	0.9600	-0.8%
50	0.95820		14.3490	0.95820	0.9700	-1.2%
56	0.97560		14.3334	0.97560	0.9780	-0.2%
60	0.99078		14.3238	0.99078	0.9890	0.2%
66	0.99476		14.3108	0.99476	0.9920	0.3%
70	0.98799		14.3033	0.98799	0.9900	-0.2%
76	1.00181		14.2944	1.00181	0.9950	0.7%
80	1.00408		14.2901	1.00408	0.9970	0.7%
86	1.00435		14.2862	1.00435	0.9980	0.6%
88	1.01497		14.2856	1.01497	1.0000	1.5%
90	1.00000		14.2855	1.00000	1.0000	0.0%

Table XI: Monte Carlo simulation results for the Anisotropy Function $F(r,\theta)$ at 2 cm from the source center and compared to results from *Daskalov et al*.[18] Results for the angle β and the Geometric function are also provided.

Anisotropy Function r=2 cm						
Monte Carlo Results					Daskalov *et al*	% Difference
Angle θ (degrees)	β	G_0	G_L	Anisotropy F(r,θ)	Anisotropy F(r,θ)	
2	0.36286	14.28546	14.4407	0.67531	0.6520	3.6%
6	1.08670		14.4392	0.70969	0.6960	2.0%
10	1.80490		14.4361	0.70778	0.7450	-5.0%
16	0.76994		14.4289	0.76994	0.8120	-5.2%
20	0.86582		14.4224	0.86582	0.8460	2.3%
26	0.92611		14.4106	0.92611	0.8990	3.0%
30	0.90060		14.4015	0.90060	0.9290	-3.1%
36	0.91914		14.3865	0.91914	0.9290	-1.1%
40	0.94308		14.3759	0.94308	0.9450	-0.2%
46	0.95214		14.3597	0.95214	0.9600	-0.8%
50	0.95820		14.3490	0.95820	0.9700	-1.2%
56	0.97560		14.3334	0.97560	0.9780	-0.2%
60	0.99078		14.3238	0.99078	0.9890	0.2%
66	0.99476		14.3108	0.99476	0.9920	0.3%
70	0.98799		14.3033	0.98799	0.9900	-0.2%
76	1.00181		14.2944	1.00181	0.9950	0.7%
80	1.00408		14.2901	1.00408	0.9970	0.7%
86	1.00435		14.2862	1.00435	0.9980	0.6%
88	1.01497		14.2856	1.01497	1.0000	1.5%
90	1.00000		14.2855	1.00000	1.0000	0.0%

Table XII: Monte Carlo simulation results for the Anisotropy Function $F(r,\theta)$ at 3 cm from the source center and compared to results from *Daskalov et al.*[18] Results for the angle β and the Geometric function are also provided.

Anisotropy Function r=3 cm						
Monte Carlo Results					Daskalov *et al*	% Difference
Angle θ (degrees)	β	G_0	G_L	Anisotropy F(r,θ)	Anisotropy F(r,θ)	
2	0.24082	6.3585747	6.3892	0.69700	0.6700	4.0%
6	0.72124		6.3889	0.73400	0.7110	3.2%
10	1.19806		6.3883	0.75739	0.7580	-0.1%
16	1.90129		6.3869	0.82902	0.8220	0.9%
20	2.35872		6.3856	0.85333	0.8540	-0.1%
26	3.02210		6.3833	0.88972	0.8890	0.1%
30	3.44601		6.3815	0.90617	0.9060	0.0%
36	4.04916		6.3786	0.94425	0.9340	1.1%
40	4.42662		6.3765	0.94389	0.9500	-0.6%
46	4.95132		6.3733	0.95499	0.9650	-1.0%
50	5.27104		6.3712	1.00252	0.9720	3.1%
56	5.70174		6.3681	0.96521	0.9800	-1.5%
60	5.95434		6.3662	0.97983	0.9850	-0.5%
66	6.27852		6.3636	0.98842	0.9850	0.3%
70	6.45672		6.3621	0.99427	0.9920	0.2%
76	6.66514		6.3604	0.99706	0.9950	0.2%
80	6.76391		6.3595	0.99631	0.9980	-0.2%
86	6.85069		6.3587	0.99643	0.9990	-0.3%
88	6.86312		6.3586	1.00059	1.0000	0.1%
90	6.86726		6.3586	1.00000	1.0000	0.0%

Table XIII: Monte Carlo simulation results for the Anisotropy Function $F(r,\theta)$ at 5 cm from the source center and compared to results from *Daskalov et al*.[18] Results for the angle β and the Geometric function are also provided.

Anisotropy Function r=5 cm						
Monte Carlo Results					Daskalov *et al*	% Difference
Angle θ (degrees)	β	G_0	G_L	Anisotropy F(r,θ)	Anisotropy F(r,θ)	
2	0.14416	2.2908419	2.29480	0.72000	0.7090	1.6%
6	0.43176		2.2948	0.73400	0.7430	-1.2%
10	0.71724		2.2947	0.79900	0.7820	2.2%
16	1.13841		2.2945	0.86060	0.8400	2.5%
20	1.41248		2.2943	0.89395	0.8720	2.5%
26	1.81016		2.2940	0.91517	0.9050	1.1%
30	2.06443		2.2938	0.93879	0.9110	3.1%
36	2.42648		2.2934	0.96310	0.9330	3.2%
40	2.65323		2.2932	0.95996	0.9450	1.6%
46	2.96868		2.2928	0.96398	0.9590	0.5%
50	3.16105		2.2925	0.97189	0.9700	0.2%
56	3.42039		2.2921	0.97808	0.9720	0.6%
60	3.57261		2.2918	0.98543	0.9790	0.7%
66	3.76809		2.2915	0.98842	0.9800	0.9%
70	3.87562		2.2913	1.00650	0.9820	2.5%
76	4.00143		2.2911	0.98608	0.9890	-0.3%
80	4.06108		2.2910	1.00059	0.9950	0.6%
86	4.11351		2.2909	0.99740	0.9980	-0.1%
88	4.12101		2.2908	1.00127	1.0010	0.0%
90	4.12352		2.2908	1.00000	1.0000	0.0%

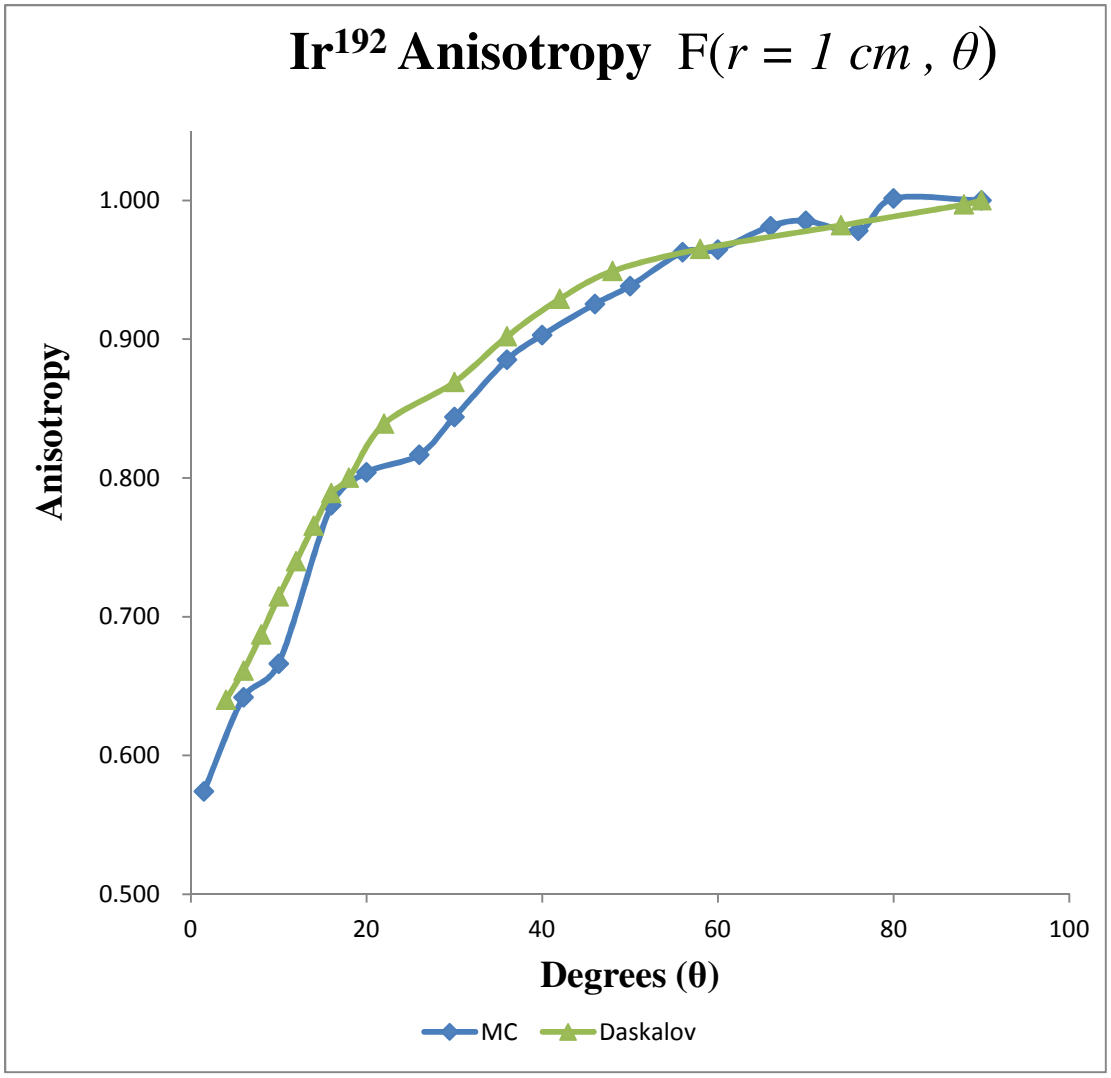

Figure 14: Plot of the Monte Carlo calculated anisotropy function from polar angle θ = 0° to 90° at a distance of 1 cm from the source center compared to values obtained by Daskalov et al.[18]

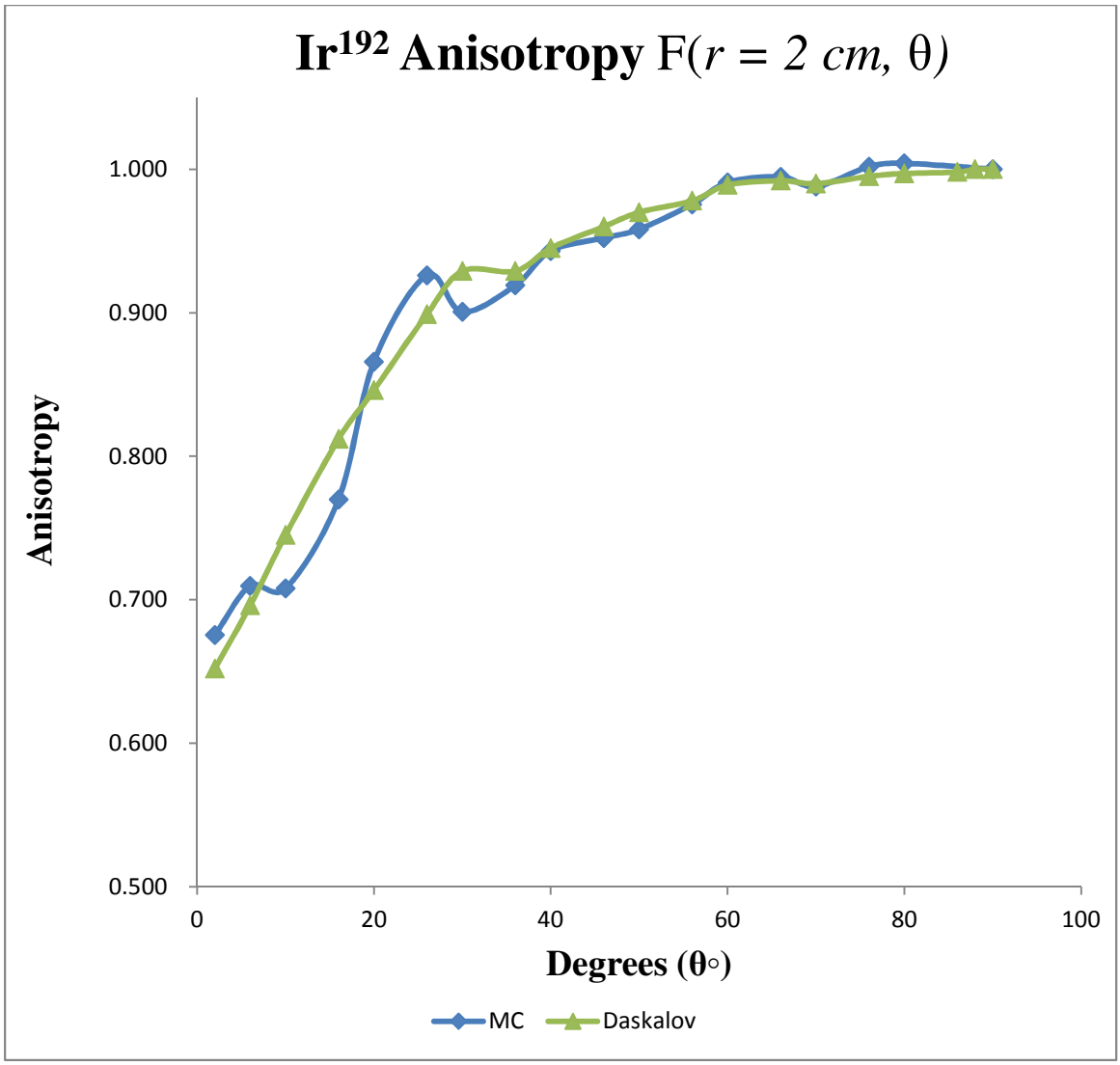

Figure 15: Plot of the Monte Carlo calculated anisotropy function from polar angle θ = 0° to 90° at a distance of 2 cm from the source center compared to values obtained by Daskalov et al.[18]

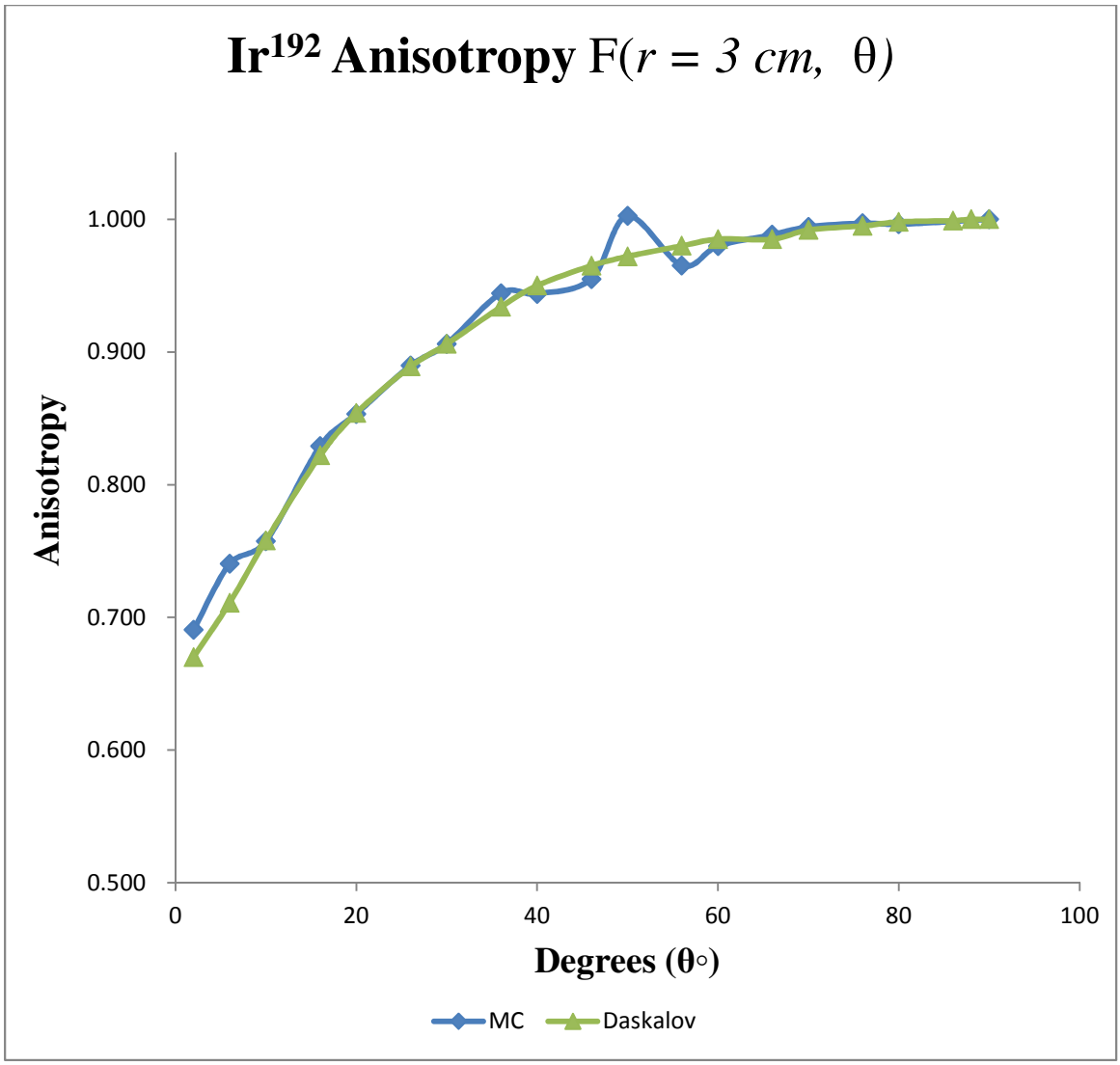

Figure 16: Plot of the Monte Carlo calculated anisotropy function from polar angle θ = 0° to 90° at a distance of 3 cm from the source center compared to values obtained by Daskalov et al.[18]

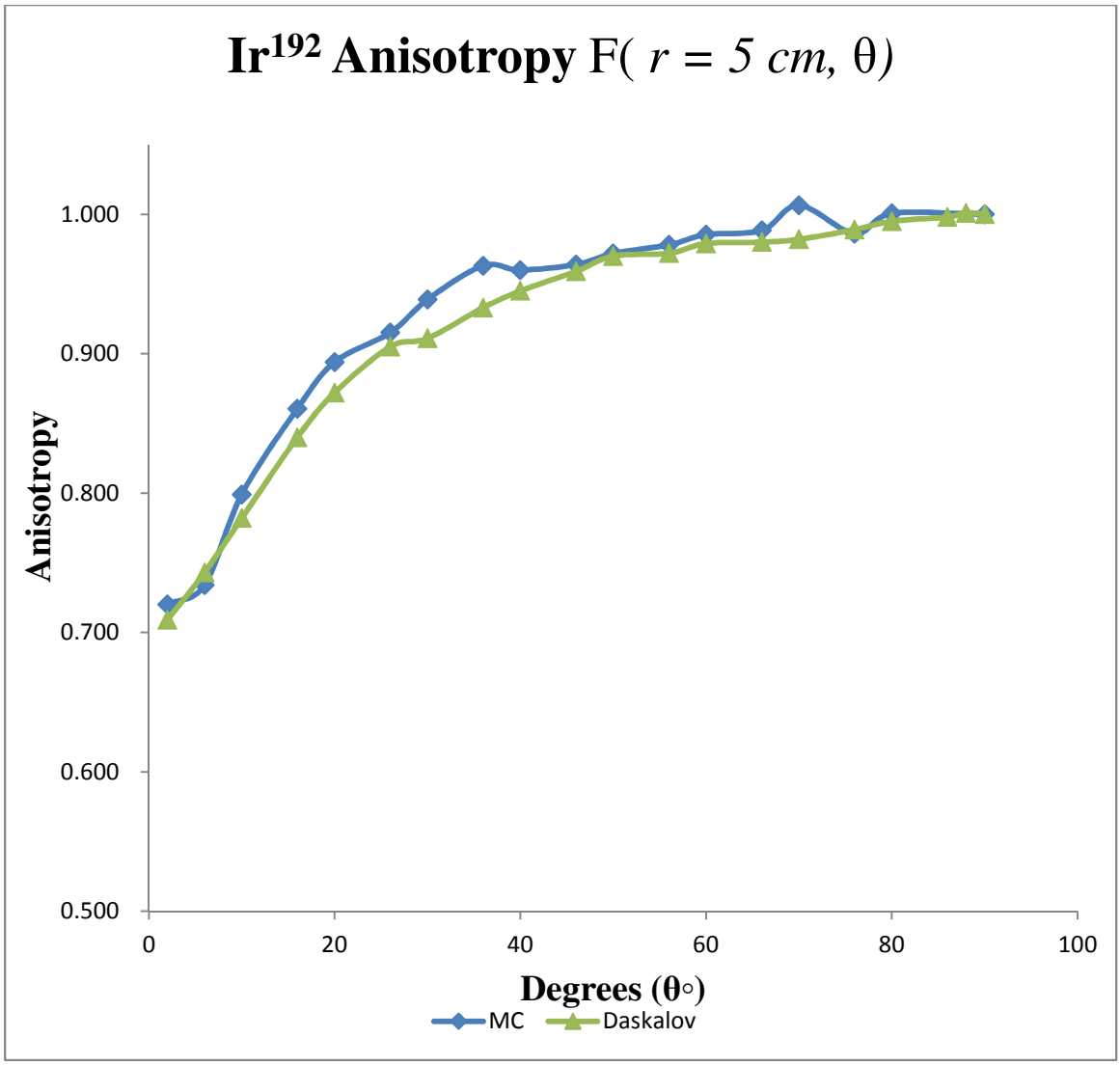

Figure 17: Plot of the Monte Carlo calculated anisotropy function from polar angle θ = 0° to 90° at a distance of 5 cm from the source center compared to values obtained by Daskalov et al.[18]

3.2 RADIAL DOSE FUNCTION

Monte Carlo results for the Radial Dose function compare very well with the results of TG-43[8,9] and *Daskalov et al.*[18] Comparison with the work of *Daskalov et al.,* has a maximum discrepancy 3.5% at 10 cm from the source and a maximum discrepancy with TG-43 of 2.4% at 0.5 cm from the source – all other values fall within 2% of the reported values for either publication.

The Monte Carlo results were plotted using Microsoft® Excel™ and a line fit was performed with a fifth degree polynomial ($R^2 = 0.9986$) to obtain the line fit required by the AAPM's TG-43. Table XV below shows the values for the calculated Geometric Function, Monte Carlo calculated Radial Dose function, polynomial fit, values from the referenced works, and per cent difference comparison with those same works. Figure 18 provides a plot of the Monte Carlo results, those for the referenced works, and polynomial fit with R^2 test. Table XVI shows the coefficient values for the polynomial fit.

The uncertainty associated with the Radial Dose Function is calculated from the formula below:

$$\sigma_{G_L}(r,\theta) = g_L \sqrt{\sigma_{MC}(r,\theta)^2 + \sigma_\mu{}^2 + (\sigma_{I_\gamma})^2}$$

In the formula above, $\sigma_{I\gamma}$ is the photon yield uncertainty of the Iridium source, calculated to be 0.5% by *Medich et al.*[19] The uncertainty varied from 5.39% at 0.5 cm from the source to 5.44% at 6 cm from the source (Table XIV.)

Table XIV: Calculated uncertainty for the Radial Dose Function at each calculated distance *r*.

r *(cm)*	% Uncertainty
0.5	5.39%
1	5.39%
2	5.41%
3	5.45%
4	5.39%
5	5.40%
6	5.44%
7	5.39%
8	5.39%
9	5.39%
10	5.42%

As it is noted in Table XV and Figure 18, that the Monte Carlo simulation for estimating the Radial Dose Function models the dose attenuation – from scattering and absorption in the medium, along the transverse bisector - sufficiently well and with a low enough discrepancy from TG-43 and *Daskalov et al.*[18] (maximum discrepancies are 2.4% and 3.5% respectively) to be accepted as valid.

Table XV: Monte Carlo calculated results for the Radial Dose Function, *R(r)*, at distances *r,* of 0.5 cm and 1 cm to 10 cm. Comparison with the values obtained by *Daskalov et al.*[18], and TG-43[8,9] are provided. The values of the Geometric Function and fitting polynomial at each distance measured are also provided.

Distance (cm)	**Go**	**G_L**	**MC *R(r)***	**Fitting Polynomial**	**Daskalov *et al.***	**% difference Daskalov**	**TG-43**	**% difference TG-43**
0.5		219.9	1.018	1.000	1.000	1.8%	0.994	2.4%
1		56.68	1.000	1.001	1.000	0.0%	1.000	0.0%
2		14.28	1.009	1.006	1.007	0.2%	1.010	-0.1%
3		6.359	1.015	1.015	1.008	0.7%	1.020	-0.5%
4		3.579	1.014	1.011	1.004	1.0%	1.010	0.4%
5	56.6	2.291	1.002	0.990	0.995	0.7%	0.996	0.6%
6		1.591	0.976	0.954	0.981	-0.5%	0.972	0.4%
7		1.169	0.953	0.908	0.964	-1.2%	0.942	1.1%
8		0.895	0.922	0.853	0.940	-1.9%	0.913	1.0%
9		0.707	0.902	0.777	0.913	-1.2%	0.891	1.2%
10		0.573	0.851	0.652	0.882	-3.5%		

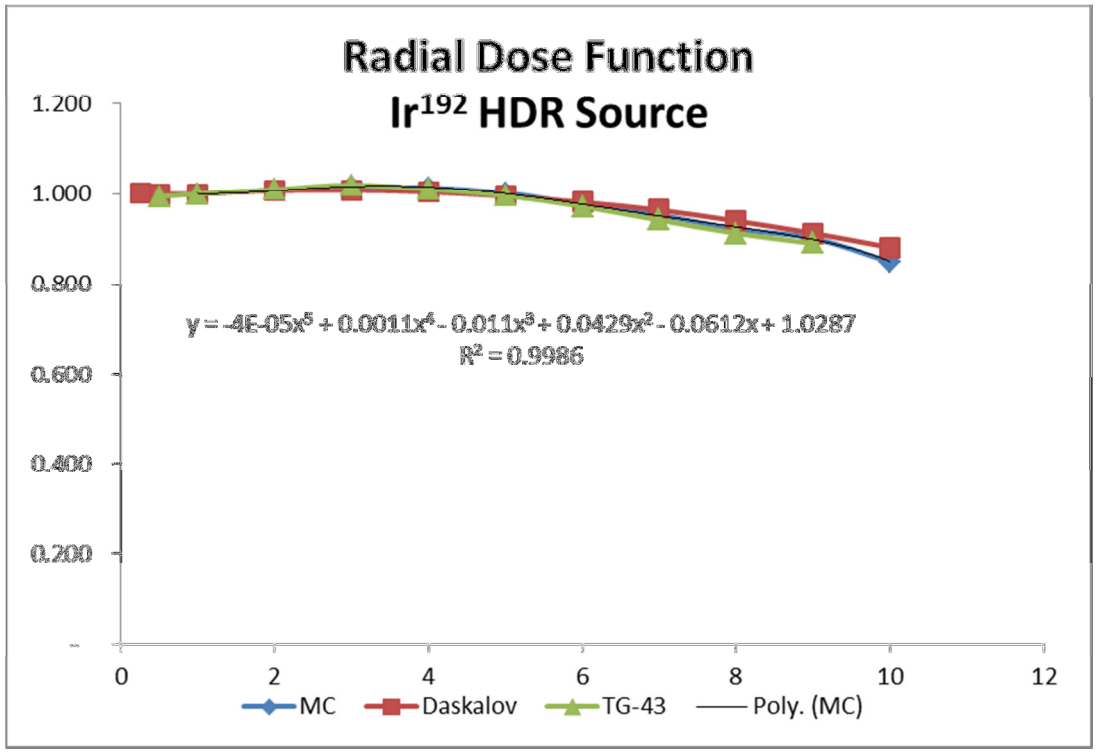

Figure 18: Plot of the Monte Carlo results for the Radial Dose Function (MC) for the simulated Iridium-192 HDR source, along with results by *Daskalov et al.*[18], and TG-43[8,9]. The fifth order fitting polynomial and R^2 of the polynomial fit are also provided.

Table XVI: Values of the coefficients for the fifth degree polynomial fit to the Monte Carlo calculated results for the Radial Dose Function.

Radial Dose Function Polynomial Fit Coefficients	
a_o	1.0287
a_1	-0.0612
a_2	0.0429
a_3	-0.011
a_4	0.0011
a_5	-0.00004

3.3 DOSE RATE CONSTANT

The Monte Carlo simulation yielded a well accepted value for the Dose Rate Constant, $\Lambda = 1.133 \frac{U}{mCi}$. This value corresponds to a relative error of 1.14% from the TG-43 calculated value of 1.12, a 2.24% relative error from the results presented by *Daskalov et al.*[18], and a 1.20% relative error from the results of *Taylor and Rogers.*[28] This error in calculated values is mainly attributed to geometric approximations in the Monte Carlo simulation and the error in the measurement of the cross-sections involved. The uncertainty in the Monte Carlo calculated value for the Air-Kerma strength is higher than in previously simulated quantities due to the relatively large distance from the source center to the

measurement point (100 cm.) Decreasing the uncertainty further would involve unavailable computational power and time; regardless, an uncertainty below 20% is generally considered acceptable for Monte Carlo simulations. The Monte Carlo calculated value for the Air-Kerma strength and uncertainty are:

$$S_{K,\delta=10KeV}\left(r=100cm,\theta_0=90°\right)=2.27\times10^7\ \frac{cGy\ cm^2}{mCi\ h}\qquad \pm15.70\%\ .$$

The measured dose-rate, in water, at a distance of 1 cm from the source center and uncertainty are:

$$\dot{D}\left(r_0=1cm,\theta_0=90^\circ\right)=2.56\times10^7\ \frac{cGy}{mCi\ h}\qquad \pm1.140\%$$

The uncertainty associated with the Air-Kerma strength and the dose-rate at 1 cm is calculated from the following respective formulas:

$$\sigma_{S_K}(r,\theta)=S_K\sqrt{\sigma_{MC}(r,\theta)^2+\sigma_\mu{}^2+\left(\sigma_{I_\gamma}\right)^2}$$

$$\sigma_\Lambda(r,\theta)=\Lambda\ \sqrt{\sigma_{MC}(r_0,\theta_0)^2+\left(\sigma_{air-\ker ma}^{\delta=10KeV}\right)^2}$$

3.4 DOSE TO SIMULATED PROSTATE

The dose-rate measurements, in the simulated Prostate, yielded results that vary significantly from the results in the homogeneous water phantom. As shown in Table XVIII, current TPS techniques over estimate the dose-rate at every point measured. At the distances of 0.5, 1 and 2.0 cm from the source center along the upper longitudinal surface of the source, a dose discrepancy, with respect to

water, is measured at -0.7%, -1.1%, and -5.6%. The opposite side of the longitudinal axis, at the same distances yields a similar over dosing of 0.6%, 1.5%, and 4.8%; the measurement at 1 cm from the distal source tip yields a dose difference of -4.6%. This result is expected due to the lower electronic density of tissue heterogeneities when compared to water. For the average energy of Iridium-192 Compton interactions are dominant, and the absorbed dose in the medium is dependent on the electronic density.

The uncertainties associated with these measurements vary from 5.45% to 6.65% and are presented in Table XVII below. The uncertainty is obtained from both the dose-rates in the simulated prostate and in the simulated water phantom.

$$\sigma_{\dot{D}(r,\theta)} = \dot{D}(r,\theta)\left(\sqrt{\left(\sigma_{MC,sim}\right)^2 + \left(\sigma_{\mu}\right)^2 + \left(\sigma_{I_\gamma}\right)^2}\right)$$

Table XVII: Uncertainty associated with dose-rate measurements in the simulated prostate.

PROSTATE		
Measurement Distance *(cm)*		Uncertainty $\sigma_{\dot{D}(r,\theta)}$
Above Source	0.5	5.45%
	1	5.63%
	2	6.65%
Tip	1	5.99%
Below Source	0.5	5.45%
	1	5.63%
	2	6.63%

Table XVIII: Comparison of the dose-rate, in the simulated Prostate from virtual phantom with heterogeneities, with the dose-rate in homogeneous water phantom. The %-difference in dose-rates shows possible discrepancies between the actual dose-rates delivered and dose-rates calculated by the TPS.

PROSTATE				
Measurement Distance *(cm)*		Dose-Rate Simulated Tissue (Dose-rate is in units of cGy mCi^{-1} h^{-1})	Dose-Rate Simulated Water (Dose-rate is in units of cGy mCi^{-1} h^{-1})	% Difference to Water
Above Source	0.5	1.59E+01	1.60E+01	-0.7%
	1	4.01E+00	4.05E+00	-1.1%
	2.0	6.47E-01	6.85E-01	-5.6%
Tip	1	1.54E+00	1.61E+00	-4.6%
Below Source	0.5	1.59E+01	1.60E+01	-0.6%
	1	3.98E+00	4.04E+00	-1.5%
	2.0	6.43E-01	6.76E-01	-4.8%

3.5 DOSE TO SIMULATED BLADDER

Dose-rates to the simulated bladder also differed significantly at every point of measurement to those in the homogenous water phantom. Each of the three measurement points in the bladder wall are grossly over estimated by the water

environment, as shown in table XX. Dose-rates at the section of the bladder wall nearest to the HDR source were overestimated in the water phantom by 14.1% and 17.1% for the outer and inner walls respectively. The midpoint between the inner and outer bladder wall furthest from the radioactive source recorded a dose over estimation, in the water phantom, of 48.9%.

Uncertainties from measurements in the bladder are presented in Table XIX below. The uncertainties are calculated by in the same manner as in the prostate case.

Table XIX: Uncertainties in dose-rate, at each measurement point in the simulated bladder.

BLADDER	
Measurement Distance *(cm)*	Uncertainty $\sigma_{\dot{D}(r,\theta)}$
Outter Wall	9.39%
Inner Wall	9.45%
Far Wall	6.23%

Table XX: Comparison of dose-rates in the simulated, Urea filled, bladder of the phantom with heterogeneities versus dose-rate in homogeneous water phantom. The %-difference in dose-rates shows possible discrepancies between the actual dose-rates delivered and dose-rates calculated by the TPS.

BLADDER			
Measurement Location	Dose-Rate Simulated Tissue (Dose-rate is in units of cGy mCi^{-1} h^{-1})	Dose-Rate Simulated Water (Dose-rate is in units of cGy mCi^{-1} h^{-1})	% Difference to Water
Outer Wall	1.61E-01	1.88E-01	-14.1%
Inner Wall	1.39E-01	1.68E-01	-17.4%
Far Wall	6.79E-03	1.33E-02	-48.9%

3.6 DOSE TO RECTUM

The simulated rectum dose-rates differ from the results in the TPS-like, homogeneous water phantom. The outer and inner walls closest to the radioactivity (Figure 13.) have an under estimation, with respect to the homogeneous water phantom of -10.4% and -14.6% respectively. The dose-rates at the furthermost rectal wall break the pattern of over estimation in part of the water phantom and yield a dose under estimation in the water environment of 5.5% and 1.2% for the inner and outer far walls respectively. The air filled cavity of the rectum allows a for a significant dose-rate increase at the far wall of the air

cavity. This increase in the dose at the far rectal wall is due to lower photon attenuation and scatter within the air filled rectal cavity when compared to water, and yields an average dose increase of 2.4% per centimeter of air. These results are in line with the results presented for the dose-rates at the lung walls from a permanent lung implant by *Y. Yang et al.*[21]

The uncertainties associated with the dose-rates in the simulated rectum vary from 9.1% to 11.9% and are presented in full in Table XXII below.

Table XXI: Comparison of dose-rates in the simulated rectum of the phantom with heterogeneities versus dose-rate in the homogeneous water phantom. The %-difference in dose-rates shows possible discrepancies between the actual dose-rates delivered and dose-rates calculated by TPS.

RECTUM			
Measurement Location	Dose-Rate Simulated Tissue (Dose-rate is in units of cGy mCi^{-1} h^{-1})	Dose-Rate Simulated Water (Dose-rate is in units of cGy mCi^{-1} h^{-1})	% Difference to Water
Outer Wall	1.66E-01	1.85E-01	-10.4%
Inner Wall	1.50E-01	1.75E-01	-14.6%
Inner Far Wall	9.09E-02	8.62E-02	5.5%
Outer Far Wall	8.73E-02	8.63E-02	1.2%

Table XXII: Uncertainties in dose-rate, at each measurement point in the simulated rectum.

RECTUM	
Measurement Distance *(cm)*	Uncertainty $\sigma_{\dot{D}(r,\theta)}$
Outter Wall	9.1%
Inner Wall	9.5%
Inner Far Wall	11.7%
Outter Far Wall	11.9%

4.0 CONCLUSIONS

Implementation of a Monte Carlo simulation for dosimetry of the widely used Nucletron Ir^{192} source (model No.105002) using MCNP5 was accomplished. The model is verified against the data provided by the American Association of Physicist in Medicine Task Group No.43 and relevant peer reviewed literature. These comparisons have yielded well acceptable results, thus allowing a conclusion that the MCNP5 based Monte Carlo model accurately simulates the Ir^{192} source and calculates dose to the desired points within the virtual phantom. We are able to insert virtual organs into the same spherical phantom and measure the influence that these organ heterogeneities have on clinical dose calculations. Comparison of dose-rates in the simulated organs versus dose-rates in the Treatment Planning System-like water method showed clinically significant differences reaching maximum discrepancies of 5.6% in the prostate, ~49% in the bladder and ~15% in the rectum. The uncertainty associated with theses measurements is within an acceptable level, allowing the conclusion that heterogeneities do to organ tissues indeed create clinically significant dose discrepancies when compared to TPS-like data.

It is recommended that further investigations be performed to quantify the influence of tissue heterogeneities on clinical doses. It would be particularly beneficial that a method for Monte Carlo based dosimetry be developed where patient CT data is used as a direct input to the particle transport calculations, similar to the methods utilized in external beam treatment planning.

REFERENCES

[1] E. J. Hall, "Radiation Biology for the Radiobiologist," Ed. 5, Ch. 5, 80-87, 2000.

[2] D. Frankenberg, M. Frankenberg-Schwager, R. Harbich, "Split-dose recovery is due to the repair of DNA double strand breaks,"Int. J. Radiat. Biol., Vol. **46**, 541-553, 1984.

[3] S. Frank, L. Pisters, J. Davis, A. Lee, R. Bassett, D. Kuban, "An Assesment of Quality of Life Following Radical Prostatectomy, High Dose External Beam Radiation Therapy and Brachytherapy Iodine Implantation as Monotherapies for Localized Prostate Cancer," The Journal of Urology, Vol. **177** (6)**,** 2151-2156, 2007.

[4] M. Ferrer, J. Suarez, J. Guedea, P. Fernandez, V. Maclas, A. Marino, A. Hervas, I. Herruzo, "Health Related Quality of Life 2 Years After Treatment with Radical Prostatectomy, Prostate Brachytherapy, or External Beam Radiotherapy in Patients with Clinically Localized Prostate Cancer," International Journal of Radiation Oncology Biology Physics, Vol. **72** (2), 421-432, 2008.

[5] S.P. Jackson, P.A. Jeggo, "DNA double-strand break repair and V(D)J recombination: Involvement of DNA-PK," T. I. B. S., Vol. **20**, 412-415, 1995.

[6]

[7] American Brachytherapy Society, "A brief Essay on the Introduction of Brachytherapy," Available at: http://www.americanbrachytherapy.org/aboutBrachytherapy/history.cfm

[8] V.K. Gupta, "Brachytherapy – past, present and future," Journal of Medical Physics, Vol. **20**, 31-38, 1995.

[9] N. Ravinder, L. L. Anderson, G. Luxton, K. A. Weaver, J. F. Williamson, A. S. Meigooni, "Dosimetry of Interstitial Brachytherapy Sources: Report of the AAPM Radiation Therapy Committee Task Group 43," Medical Physics, Vol. **22**, 1995.

[10] M. J. Rivard, B. M. Coursey, L.A. DeWerd, W. F. Hanson, M. S. Huq, G.S. Ibbott, M. G. Mitch, R. Nath, J. F. Williamson, "Update of AAPM Task Group No.43 Report: A revised AAPM Protocol for brachytherapy dose calculations,"Med. Phys. Vol. **31**(3), 2004.

[11] M. J. Rivard, W.M. Butler, L. A. DeWerd, M. S. Huq, G. S. Ibbott, A. S. Meigooni, C. S. Melhus, M. G. Mitch, R. Nath, J. F. Williamson, "Supplement to the 2004 Update of the AAPM Task Group No.43 Report," Med. Phys., Vol. **34**(6), 2007.

[12] International Comission on Radiation Units and Measurements,"Fundemental Quantities and Units for Ionizing Radiation (ICRU Report No.60,)" Vol. **60**, 13-14, 1998.

[13] M. Shlomo, S. Mordechai, "Applications of Monte Carlo in Science and Engineering," 1-20, 35-48, 2011.

[14] S. Weinzierl, “Introduction to Monte Carlo Methods.” Available at: http://arxiv.org/abs/hep-ph/0006269v1.

[15] Los Alamos Science Special Issue,“The Beginnig of the Monte Carlo Method,” 1987.

[16] N. Metropolis, S. Ulam, “The Monte Carlo Method,” Journal of American Statistical Society, Vol. **44**, 335-341, 1940.

[17] F. B. Brown *et al,* “MCNP – A General Monte Carlo N-Particle Transport Code, Version 5: Overview and Theory,” Los Alamos National Laboratory, 2003.

[18] M. E. Battat *et al,* “ANS-6.1.1 Working Group: Neutron and Gamman-Ray Fluence-To-Dose Factors,” American Nuclear Society, 1991.

[19] M. Daskalov, J. F. Williamson, “Monte Carlo-Aided Dosimetry of a new high dose-rate brachytherapy source,” Med. Phys. Vol.**25**(11), 1998.

[20] M. J. Rivard, “Influence of Photon Energy Spectra from Brachytherapy Sources on Monte Carlo Simulations of Kerma and Dose-Rates in Water and Air,” Med. Phys. Vol. **37**(2), 2010.

[21] D. C. Medich, J. J. Munro III, “Monte Carlo Characterization of the M-19 high dose rate Iridium-192 brachytherapy source,” Med. Phys. Vol. **34** (6), 2007.

[22] Y. Yang, M. J. Rivard, “Evaluation of brachytherapy lung implant dose distributions from photon-emitting sources due to tissue heterogeneities,” Med. Phys. Vol.**38** (11), 2011.

[23] D. Granero, J. Vijande, F. Ballester, M. J. Rivard, "Dosimetry revisited for the HDR ^{192}Ir brachytherapy source model mHDR-v2. Med. Phys. Vol. **38** (1), 20011.

[24] R. P. King, "Geometric function of a linear brachytherapy source," Journal of Applied Clinical Medical Physics, Vol.**2** (2), 2001.

[25] National Institute of Standards and Technology,"X-Ray Mass Attenuation Coefficients," Available at: http://physics.nist.gov/PhysRefData/XrayMassCoef/tab3.html .

[26] Jean-Francois Carrier, L. Beaulieu, "Impact of interseed attenuation in tissue composition for permanent prostate implants," Med. Phys. Vol. **33** (3), 2006.

[27] International Comission on Radiation Units and Measurements. "Measurement of Dose Equivalent from External Photon and Electron Radiations (ICRU Report No.47,)" Vol. **47**, 401-466, 1992.

[28] H. R. Yun, H. Chun, W. S. Lee, Y. B. Cho, S. H. Yun, W. Y. Lee, "Intra-operative Measurement of Surgical Lengths of the Rectum and the Peritoneal Reflection in Korean," J. Korean Med. Sci., Vol. **23** (6), 2008.

[29] "EGSnrc Monte Carlo calculated dosimetry parameters for ^{192}Ir and ^{169}Yb brachytherapy sources," Med. Phys., Vol. **35** (11), 4933–4944, 2008.